Supplement to "Version 2 data of the National Science Foundation's Ultraviolet Radiation Monitoring Network: South Pole"

G. Bernhard, C.R. Booth, and J.C. Ehramjian

Biospherical Instruments Inc., San Diego

For clarity, the section numbering in this supplement is consistent with that of the 'main' part of the paper and prefixed with a capital S.

S1. Introduction

Application of data from the NSF/OPP UV network

Network data has been used by dozens of researchers investigating the relationship between solar UV irradiance and total ozone [*Díaz et al*., 1994*; Bojkov et al.*, 1995; *Booth et al., 1994; Booth and Madronich*, 1994]; the effect of the "ozone hole" on UV irradiance [*Lubin et al.*, 1989; *Frederick and Alberts*, 1991; *Stamnes et al*., 1992; *Frederick et al*., 1993]; variability of UV on various time scales [*Díaz et al*., 1996; *Sobolev*, 2000; *Frederick et al*., 2001; *Frederick and Liao*, 2003]; geographical differences in UV [*Seckmeyer et al*., 1995]; trends in UV radiation [*Gurney*, 1998; *Díaz et al*., 2003]; separation of the effects of ozone, cloudiness and surface albedo on UV [*Chubarova et al*., 1997; *Díaz et al*., 2001]; the effect of high-latitude clouds on UV [*Frederick and Erlick*, 1997]; moderation of cloud attenuation by albedo [*Nichol et al*., 2003]; and the effect of the quasi-biennial oscillation (QBO) on UV [*Zerefos et al.*, 2001]. Network data was further used to study the general effects of Antarctic ozone depletion on the biota [*Lubin et al*., 1992]; the effects of UV radiation on aquatic ecosystems [*Cullen et al.*, 1992; *Smith et al.*, 1992 *Holm-Hansen et al.*, 1993; *Boucher and Prézelin*, 1996; and *Díaz et al*., 2000], plants [*Day et al*., 1998], and photoproduction of vitamin D3 [*Ladizesky et al*., 1995]. In addition, network data were used for validation of satellite observations [*Kalliskota et al*., 2000]; comparison with radiative transfer models [*Frederick et al*., 1993; *Gardiner and Martin*, 1997; *Nichol et al*., 2003]; comparison with Dobson photometer ozone observation [*Bernhard et. al*., 2003b]; comparison with data from other UV spectroradiometers [*Early et al*., 1998; *Dahlback*, 1996; *Bais et al.*, 2001; *Lantz et al*., 2002], and in scientific assessments of ozone depletion published by the World Meteorology Organisation (WMO) [*WMO*, 1999; 2003].

S2. Corrections

S2.1. Radiative transfer model

S2.1.2. Extraterrestrial spectrum. At the time of this writing, there is no consensus on the extraterrestrial spectrum (ETS) best suited for modeling in the UV and visible. We therefore developed a new ETS for Version 2 processing, which combines the advantages of three commonly used ETS. This ETS is a composite of the spectra measured by the Solar Ultraviolet Spectral Irradiance Monitor (SUSIM) onboard the space shuttle during the ATLAS-2 and 3 missions [*Kaye and Miller*, 1996; *vanHoosier*, 1996], and the very high-resolution (approximately 0.0001 nm) "Kitt Peak solar flux atlas" [*Kurucz et al.*, 1984], measured with a Fourier Transform Spectroradiometer. The Kitt Peak spectrum covers the range 296-1300 nm, and is reported in "air" wavelengths. We verified its wavelength accuracy to be better than 0.001 nm by comparing the position of its Fraunhofer lines with the wavelengths of tabulated electronic transitions. The spectrum was convolved with a triangular slit function of 0.05 nm, and is denoted $E_K(\lambda)$.

The SUSIM/ATLAS-3 spectrum covers the range 200-407.8 nm. Its radiometric uncertainty has been analyzed by several groups, and is believed to be better than ±2% in the UV-A and UV-B (e.g. [*Gröbner and Kerr*, 2001]). Its spectral resolution is about 0.15 nm. It is given in "vacuum" wavelengths and was shifted to "air" wavelengths before use.

The composite ETS used in our model calculations is denoted $E_*(\lambda)$ and combines the good radiometric accuracy of SUSIM with the superior wavelength accuracy and resolution of Kitt Peak. It was constructed as follows:

- Below 298.4 nm, $E_*(\lambda)$ is SUSIM/ATLAS-3, shifted to air wavelength
- Between 298.4 nm and 338.5 nm, $E_*(\lambda)$ was calculated by

$$E_*(\lambda) = \frac{E_K(\lambda)\ \tilde{E}_{A3}(\lambda)}{\tilde{E}_K(\lambda)} \tag{S1}$$

where $\tilde{E}_{A3}(\lambda)$ is SUSIM/ATLAS-3, shifted to air wavelengths, and smoothed with an approximating spline, and

$\tilde{E}_K(\lambda)$ is $E_K(\lambda)$, smoothed with an approximating spline.

The smoothing with the approximating spline produces a result similar to convolution with a triangular function with 0.7 nm FWHM. The construction preserves the absolute calibration of SUSIM/ATLAS3 and the wavelength calibration of $E_K(\lambda)$, but removes an anomaly in $E_K(\lambda)$ located between 320 and 330 nm.

- Between 338.5 and 407.8 nm, $E_*(\lambda)$ was calculated with Eq. (S1), but applying a stronger spline-smoothing than used for the previous interval. The smoothed functions are similar to results obtained with a 4.0 nm FWHM convolution.
- Between 407.8 and 419.9 nm, $E_*(\lambda)$ was calculated with Eq. (S1), strong smoothing, and SUSIM/ATLAS-2 rather than SUSIM/ATLAS-3.
- Between 419.9 and 620.0 nm, $E_*(\lambda)$ is identical to $E_K(\lambda)$.

The composite spectrum $E_*(\lambda)$ is specified in air wavelengths at standard pressure (1013.25 hPa) and used without adjustment (i.e. no shift of 0.03 nm at 300 nm was applied) for the actual air pressure at South Pole (680 hPa on average). Since the spectrum also serves as reference spectrum for the wavelength correction procedure outlined in Section S2.2., corrected Version 2 spectra also refer to air wavelengths at standard pressure. Although technically incorrect, the omission of air pressure correction has several advantages. For example, spectra measured at different pressure or at sites with different altitude can be directly compared. Furthermore, it is not necessary to adjust the wavelength scale of action spectra, which describe the wavelength dependence of biological effects, to the actual air pressure at the measurement site: when both the measured spectrum and the action spectrum are based on air wavelengths, the weighted integral is the correct result.

S2.2. Wavelength Shift Correction

Most of the fine structure in solar UV and visible spectra is caused by the Sun's Fraunhofer lines. As their position is accurately known, the structure can be used to determine wavelength shifts in measured spectra. This method has been successfully used by several researchers [*McKenzie et al*., 1992; *Huber et al*., 1993; *Slaper et al*., 1995; *Liley and McKenzie*, 1997; *Mayer*, 1997] and was also used for the preparation of Version 2 data. In our implementation, we compare the structure in measured spectra with corresponding structure in modeled spectra.

Differences between measurement and model that are not caused by wavelength shifts may introduce errors into the shift analysis. It is therefore necessary to remove these differences before starting the correlation. In our implementation, we first apply smoothing to both the measured and modeled spectrum and correlate the ratio of original and smoothed measured spectrum against the ratio of original and smoothed model spectrum. This method is similar to the one used by *Mayer* [1997], and is illustrated in Figure S1.

For determining a smoothed spectrum, the logarithm of the original spectrum is calculated, the result is then smoothed by an approximating spline, and the exponential of the spline function is determined. (The smoothed spectrum is similar to a spectrum that is obtained by convolving the log-spectrum with a 8-nm wide triangular function before calculating the exponential. The approximating spline however better matches the slope of the solar spectrum in the ozone cut-off region than the convolved spectrum.) The ratio of original and smoothed spectrum is very similar for the measured and modeled data sets, as Figure S1 demonstrates, but both ratio-spectra are slightly shifted against each other. The correlation is finally performed by calculating the wavelength shift δ that leads to a minimum of the error ratio $E_R(\delta)$, defined as:

$$E_R(\delta) = \sqrt{\frac{\sum_{\lambda_m \in [\lambda_C - \lambda_I, \lambda_C + \lambda_I]} \left(\frac{r_M(\lambda_m)}{r_C(\lambda_m + \delta)} \right)^2}{m-1}} \qquad \text{(S2)}$$

where λ_m are the discrete wavelengths of the measured spectrum,
λ_C is wavelength for which the wavelength shift is calculated,
λ_I is the half-width of the correlation interval,
δ is the wavelength shift, given in multiples of 0.01 nm,
$r_M(\lambda)$ is the ratio of the original and smoothed measured spectrum,
$r_C(\lambda)$ is the ratio of the original and smoothed modeled spectrum given in steps of 0.01 nm, and
m is the number of wavelengths λ_m in the interval $[\lambda_C - \lambda_I, \lambda_C + \lambda_I]$.

The precision of wavelength shifts determined with this method is limited to 0.01 nm, which is the resolution of the model spectrum. In order to get a stable result, the sum of Eq. (S2) has to be based on a sufficiently large number addends *m*. This number also controls λ_I, and depends on the wavelength resolution of the measured spectrum. When measured spectra were oversampled (wavelength resolution 0.5 nm or smaller), λ_I was set to 3.0 nm. In the visible, λ_I was set to 15.0 nm. The larger interval is required as spectra were typically measured in 1.0 nm resolution (slight undersampling) and the Fraunhofer structure is less pronounced in the visible than in the UV. When λ_I was set to 30 nm, the algorithm also proved stable for spectra from the first half of 1991, which were measured with 5.0 nm resolution in the visible. Irregularities in the monochromator's wavelength mapping that only affect a small wavelength range can obviously not be corrected if λ_I is large. Wavelength shifts in Version 0 data may change by 0.1 nm on a scale of 20 nm in some years. Shifts on this scale can be handled by the algorithm in most cases.

The algorithm cannot be applied to wavelengths close to the detection limit. The shortest wavelength where the algorithm delivers reliable results varies between 302.5 and 307.5 nm, depending on solar zenith angle and total

column ozone. Shifts below the cut-off wavelength are determined by extrapolation.

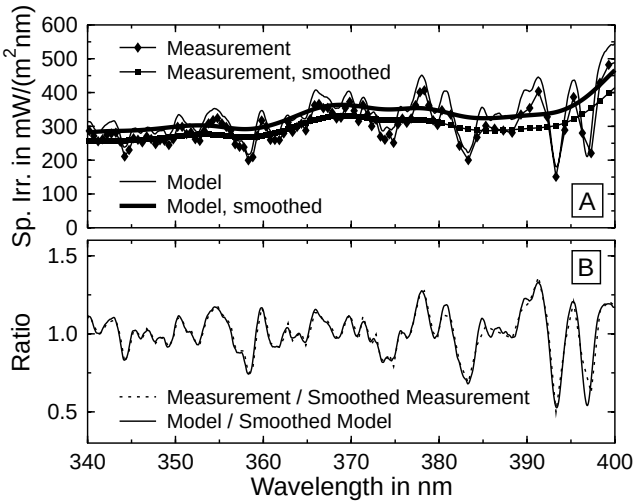

Figure S1. Illustration of wavelength correlation algorithm. (A) Original and smoothed measured and modeled spectra. (B) Ratios of original to smoothed data sets used for the correlation.

Determining wavelength shifts for all measured spectra is computationally demanding. For processing Version 2, wavelength shifts were calculated for one spectrum per day, and averaged over periods ranging from one day to several months. Using an average also eliminates the risk that a spectrum is wrongly corrected when the algorithm is disturbed by rapidly changing irradiance levels during the recording of the spectrum. This does occasionally occur under changing cloud conditions.

Spectra are finally corrected by adding the average wavelength shifts determined with the correlation algorithm to the spectra's wavelength column. Remapping of wavelength to an evenly spaced wavelength grid is described in Section S2.4. All corrected spectra are checked for wavelength shifts by applying the algorithm a second time, and the results are used to flag spectra that do not meet certain criteria.

Below 440 nm, Version 0 spectra from Volume 7 on have already been corrected for wavelength errors using the correlation algorithm by *Slaper et al*. [1995], as described in Network Operations Reports (e.g. [*Bernhard et al*., 2003a]). The algorithm was examined during several intercomparison campaigns [*Slaper*, 1997; *Slaper and Koskela*, 1997] involving a large variety of instruments, and was found to be accurate to within ±0.02 nm (±2σ) [*Slaper and Koskela*, 1997]. The Version 2 algorithm was validated by calculating the shifts of Version 0 spectra that have already been corrected with the algorithm by *Slaper et al*., [1995]. We determined the average wavelength bias between both methods to be 0.003±0.018 nm (±1σ) in the UV. This difference is within the uncertainty of the method by *Slaper et al*. [1995]. Some of the variation may be explained by the different setting of the correlation interval, as λ_I was set to 5 nm in the Version 0 implementation and to 3 nm for Version 2 processing. We did not use the *Slaper et al*. [1995] method for Version 2 since our algorithm can be better optimized for the specific requirements of our data format and sampling scheme (e.g. undersampling of early data).

S2.3. Cosine Error Correction

Before modifying the irradiance collector of the SUV-100 spectroradiometer in January 2000, the angular response of the system was dependent on wavelength and the azimuth position of the light source (lamp or Sun) illuminating the collector. The original collector consisted of a diffuser made of polytetrafluorethylene (PTFE), which has trapezoidally shaped walls [*Bernhard et al.*, 2003a]. The raised walls lead to a reduced cosine error by compensating reflection losses at large incidence angles. Similar designs are frequently implemented in contemporary diffusers [*Harrison et al.*, 1994; *Bernhard and Seckmeyer*, 1997]. The walls are brighter at the side facing the light source, which lead to a different illumination of the monochromator's gratings depending on the azimuth angle of the Sun. The modified collector has an aperture behind the diffuser which prevents radiation originating from the diffuser walls from entering the monochromator. The modification virtually eliminated the azimuth asymmetry, but lead to increased cosine errors.

The wavelength dependence of the angular response was caused by anomalies in the efficiency of the monochromator's gratings (Wood's anomalies [*Palmer*, 2002]) and the sensitivity of the wavelength of these anomalies to the angular distribution of radiation entering the monochromator from the collector. This was the case before the aperture was installed.

S2.3.1. Measurement of the SUV-100 cosine error. The cosine error of radiometers is usually characterized in the laboratory by using a lamp to illuminate the instrument under test at different zenith and azimuth angles [*Webb et al.*, 1994]. This approach is not feasible for the SUV-100 spectroradiometer at South Pole (SPO) as the instrument is assembled into a specially designed roof-box and the cosine response was found to differ when the instrument was periodically re-furbished and re-assembled. To overcome this problem, we have built an apparatus that allows characterizing the angular response of the instrument at its place of deployment. It consists of a light source, which is coupled via an optical fiber bundle and a lens assembly into a baffled tube. The tube threads into a black anodized cylinder, which has precisely machined openings at 0°, 30°, 45°, 60°, and 70° zenith angles (ZA). For measuring the angular response, the cylinder is placed on top of the instrument's collector. By coupling the tube to the different openings and turning the apparatus to different azimuth angles the angular response can be measured at five zenith angels and arbitrary azimuth angles. During the instrument inspection in January 2000,

a prototype apparatus was used, which had openings at 0° and 70° zenith angle only. A picture of this system is shown and further described by *Bernhard et al.* [2003c].

The final apparatus with five openings was available after March 2000. Figure S2 shows the angular response measured with this system at SPO in January 2001, in comparison with similar measurements at Palmer Station, and San Diego. All measurements were performed with the modified collector. Measurements at all sites agree to within ±2.2%. Observed variations with azimuth angle were smaller than ±2% at ZA = 70°.

The test apparatus is limited to measurement of the cosine response for zenith angles up to 70°. Cosine errors at larger angles were determined by using the Sun as light source, as described in Section S2.3.2.

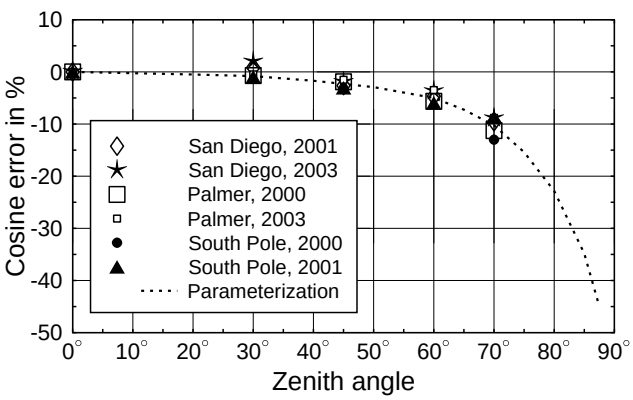

Figure S2. Cosine error ($f_B(\theta)$ - 1) of SUV-100 spectroradiometers with modified collector. The symbols represent measurements with the cosine test apparatus. The parameterization indicated by the dashed line was established with South Pole data from 2000 by comparing measured and modeled irradiance at 600 nm as explained in the text.

S2.3.2. Cosine correction for clear sky conditions. The effect of the cosine error on solar measurements is described in several publications [*McKenzie et al*., 1992; *Seckmeyer and Bernhard*, 1993; *Gröbner et al*., 1996, *Bais et al*., 1998; *Bernhard and Seckmeyer*, 1999]. The ratio f_G of measured global irradiance affected by this error to the true global irradiance can be expressed by the following equation:

$$f_G(\theta,\lambda) = f_B(\theta,\lambda)\ R(\theta,\lambda) + f_D(\lambda)\ [1 - R(\theta,\lambda)], \quad \text{(S3)}$$

where θ is solar zenith angle (SZA),

λ is wavelength,

$f_B(\theta,\lambda)$ is the cosine error, defined here as the ratio of measured to true irradiance from the Sun's direct beam on a horizontal surface,

$f_D(\lambda)$ is the diffuse cosine error, defined as the error in measuring isotropic radiance originating from the upper hemisphere:

$$f_D(\lambda) = \frac{\int_{(2\pi)} f_B(\theta,\lambda)\ \cos(\theta)\ d\Omega}{\int_{(2\pi)} \cos(\theta)\ d\Omega}$$

where Ω is solid angle, and

$R(\theta,\lambda)$ is the ratio of beam irradiance on a horizontal surface, $E_B(\theta,\lambda)$, and global irradiance $E_G(\theta,\lambda)$:

$R(\theta,\lambda) = E_B(\theta,\lambda)/E_G(\theta,\lambda)$.

For clear sky conditions, $R(\theta,\lambda)$ is estimated with the radiative transfer model. For the definition of $f_D(\lambda)$, we assumed that sky radiance is isotropic. Uncertainties related to this assumption are discussed in Section S3.2.

At 600 nm, global irradiance is dominated by the direct solar beam. This makes it feasible to use the Sun as light source for determining $f_B(\theta,\lambda)$. We implemented this approach by comparing global irradiance at 600 nm during clear skies with results of the radiative transfer model. The approach assumes that the model correctly calculates global irradiance at 600 nm. If this is the case, $f_G(\theta,600\text{nm})$ becomes equal to the ratio of measurement and model, denoted $q(\theta,600\text{nm})$. Uncertainties of this approach are discussed in Section S3.2. We calculated $f_B(\theta,\lambda)$ for $\lambda = 600$ nm by resolving Eq. (S3) for $f_B(\theta,\lambda)$ and setting $f_G(\theta,600) = q(\theta,600)$. Characterization with the test apparatus after the collector upgrade did not indicate any significant dependence of the collector's angular response on wavelength. It is therefore possible to set $f_B(\theta,\lambda) = f_B(\theta,600\text{nm})$. The cosine error $f_B(\theta,\lambda)$ calculated with this method from data of the year 2000 is indicated by the dashed line in Figure S2.

The azimuth dependence of the cosine error prior to January 2000 required a further modification of the method of estimating $f_B(\theta,\lambda)$. We approximate the azimuthal dependence of $f_B(\theta,\lambda)$ by:

$$f_B(\theta,\lambda,\varphi) \approx \quad \text{(S4)}$$

$$f_{B,\text{approx}}(\theta,\lambda,\varphi) = a(\theta,\lambda) + b(\theta,\lambda)\sin(\varphi + c(\theta,\lambda)),$$

where φ is solar azimuth angle, and

a, *b* and *c* are empirically derived coefficients depending on θ and λ.

In order to determine the coefficients *a*, *b* and *c*, clear sky spectra were binned into SZA-intervals of ±0.5° and compared with the clear sky model at several wavelengths. Setting again $f_G(\theta,\lambda,\varphi) = q(\theta,\lambda,\varphi)$, and placing Eq. (S3) into Eq. (S4) leads to the following relationship:

$$a(\theta,\lambda)+b(\theta,\lambda)\sin(\varphi+c(\theta,\lambda))\approx \frac{q(\theta,\lambda,\varphi)-f_D(\lambda)\ [1-R(\theta,\lambda)]}{R(\theta,\lambda)}. \quad \text{(S5)}$$

The coefficients *a*, *b* and *c* for each SZA bin and wavelength are determined by non-linear fits, correlating the right side of Eq. (S5) against φ. $f_D(\lambda)$ is not known at the time of the fit. It is initially set to 0.94 and then iteratively calculated more accurately: after determining preliminary values for $a(\theta,\lambda)$, a new value for $f_D(\lambda)$ is calculated and the fit repeated. Figure S3 shows a comparison of $f_B(\theta,\lambda,\varphi)$ as calculated from the right side of Eq. (S5) and the associated fit function $f_{B,\text{approx}}(\theta,\lambda,\varphi)$ for θ=70° and λ=400 nm, demonstrating that the parameterization of Eq. (S4) is suited to express the azimuth dependence of $f_B(\theta,\lambda,\varphi)$.

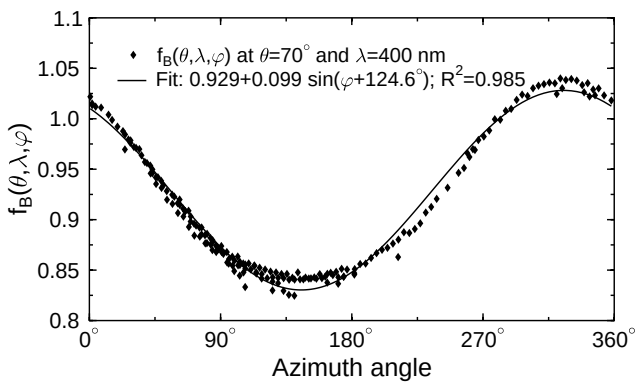

Figure S3. Cosine error $f_B(\theta,\lambda,\varphi)$ at $\theta=70°$ and $\lambda=$ 400 nm as a function of azimuth angle, determined from the difference of measured and modeled global irradiance spectra (diamonds). The solid line indicates the associated fit-function.

The coefficients $a(\theta,\lambda)$, $b(\theta,\lambda)$, and $c(\theta,\lambda)$ are smooth functions of θ, and are approximated by polynomials:

$$\begin{aligned} a(\theta,\lambda)&=u_0(\lambda)+u_1(\lambda)\theta+u_2(\lambda)\theta^2+u_3(\lambda)\theta^4\\ b(\theta,\lambda)&=v_0(\lambda)+v_1(\lambda)\theta+v_2(\lambda)\theta^2+v_3(\lambda)\theta^4\\ c(\theta,\lambda)&=w_0(\lambda)+w_1(\lambda)\theta+w_2(\lambda)\theta^2 \end{aligned} \quad \text{(S6)}$$

The coefficients $u_i(\lambda)$, $v_i(\lambda)$, and $w_i(\lambda)$, with $i=0,1,2,3$ are determined by regression against θ. As shown below, there is no evidence that $a(\theta,\lambda)$ is wavelength dependent. We therefore set $u_i(\lambda)=u_i(600\text{ nm})$. In contrast, $v_i(\lambda)$ and $w_i(\lambda)$ cannot be approximated by simple analytical functions of λ. The coefficients are calculated at discrete wavelengths, and values for other wavelengths are determined by linear interpolation. The wavelength dependence of $v_i(\lambda)$ and $w_i(\lambda)$ is caused by the monochromator's Wood anomalies.

One caveat of the approach using a measurement/model comparison for the determination of the $f_B(\theta,\lambda,\varphi)$ is that the measurement is forced to agree with model values, which are not necessarily correct. This issue is not problematic for coefficients *b* and *c*, which express the amplitude and phase of the azimuth dependence, respectively, since real atmospheric processes do not vary sinusoidally with the azimuth angle at SPO. (Otherwise solar measurements with the modified collector would show similar artifacts, which is not the case.) In contrast, coefficient $a(\theta,\lambda)$ corrects for general level-differences between measurement and model, which may be caused by model errors, inappropriate model input parameters, or systematic errors in the measurement.

We checked the model-based parameterization of $f_B(\theta,\lambda,\varphi)$ for the original collector design by comparison with angular response measurements obtained with the test apparatus. As an example, Figure S4 shows $f_B(\theta,\lambda,\varphi)$ versus wavelength at $\theta=70°$ for three azimuth angles. The drop in the response at 505 nm is caused by a Wood anomaly, and is well reproduced by both measurement and parameterization. At $\varphi=0°$, the agreement of both data sets is almost ideal. At $\varphi=180°$ and 270°, there is a difference of about 2%. This reasonably good agreement indicates that the model-based approach is feasible for determining the instrument's cosine and azimuth errors. Below 330 nm, the measurement becomes unreliable due to low signal levels. Below this wavelength, the parameterization is also problematic, partly because of the small values of $R(\theta,\lambda)$ and partly because of the increasing influence of ozone absorption.

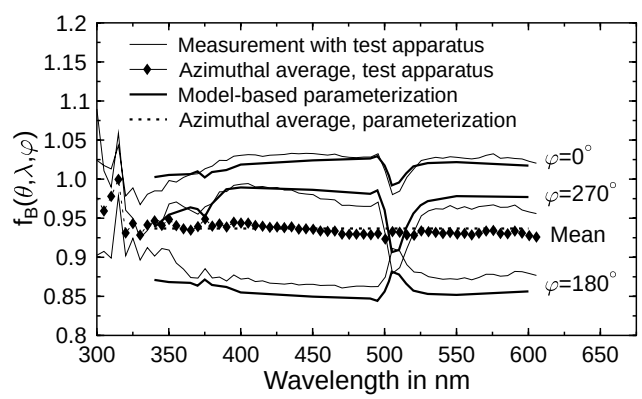

Figure S4. Cosine error $f_B(\theta,\lambda,\varphi)$ at $\theta=70°$ as a function of wavelength for the azimuth angles φ = 0°, 180°, and 270°. Thin lines indicate results obtained from measurements with the test apparatus during the site visit at the South Pole in January 2000. Thick lines are based on the parameterization using a set of coefficients $u_i(\lambda)$, $v_i(\lambda)$, and $w_i(\lambda)$. The lines labeled "Mean" give the azimuthally averaged cosine error based on measurement and parameterization.

We calculated the mean cosine error at $\theta = 70°$, by averaging the test apparatus results over all azimuth angles (broken line with triangles in Figure S4). The error is almost independent of wavelength and on average –6.5%. This confirms the previous assumption that $a(\theta,\lambda)$ is independent of λ. The average cosine error at 70° of the parameterization is –6.3%, and independent of wavelength by construction. The good agreement between measured and parameterized cosine error validates the procedure.

The cosine correction of a clear sky solar spectrum is finally performed by dividing the measured global spectral irradiance with $f_G(\theta,\lambda)$.

S2.3.3. Cosine correction for cloudy conditions. Clouds lead to a spatial redistribution of radiation. The involved processes are too complex to be considered in an exact manner, and simplifications are required. For the correction algorithm we assume that clouds at SPO are homogeneous, stratiform, made of ice crystals, and can be parameterized by a lower and upper boundary and cloud optical depth (COD) τ. In brief, the algorithm estimates τ by comparing measured global irradiance under clouds at 450 nm with the associated clear sky model spectrum. The method is similar to that presented by *Leontyeva and Stamnes* [1993]. We use a wavelength in the visible rather than UV, as visible radiation is more effectively attenuated by clouds (Section 6.1). This is particularly important for places with high albedo, such as SPO, where high albedo mitigates cloud attenuation [*Frederick and Erlick*, 1997; *Nichol et al*., 2003]. For example, model calculations for $\theta = 75°$ at the South Pole indicate that an ice cloud with τ=0.3 leads to a 7% attenuation of global irradiance at 350 nm and 14% at 450 nm. Despite the comparatively small effect on global irradiance, clouds lead to pronounced reduction of the direct to global ratio: $R(75°, 350\,\text{nm}, \tau)$ is 0.259 for τ=0 but only 0.087 for τ=0.3. Above 450 nm, ozone absorption in the Chappuis band becomes important. As absorption in the Chappuis band is not included in the "cloud" model , we chose 450 nm for COD determination rather than a longer wavelength, which would have even greater sensitivity to clouds. Under scattered clouds with the Sun unobscured, the measured irradiances may exceed the clear sky model. In this case, τ was set to zero and the clear-sky cosine correction was applied.

In the second step of the cloud cosine correction algorithm, the ratio of direct and global irradiance $R(\theta,\lambda)$ is calculated with the radiative transfer model using the previously-established cloud optical depth as an additional input parameter. The procedure is an extension of a method proposed by *Fioletov et al*., [2002]. For large cloud optical depths, $R(\theta,\lambda)$ approaches zero, Eq. (S3) simplifies to $f_G(\theta,\lambda) = f_D(\lambda)$, and $f_G(\theta,\lambda)$ becomes independent of θ. There is no evidence that the diffuse cosine error $f_D(\lambda)$ of SUV-100 spectroradiometers is wavelength dependent. Spectra measured under optically thick clouds are corrected by scaling measured global irradiance with the constant factor of $1/f_D$. The algorithm has been explained in greater detail by *Bernhard et al*. [2003c].

S2.3.4. Validation of cosine correction algorithm. Figure S5 shows the result of the cosine correction algorithm for four spectra measured during clear skies (upper panels), during the presence of a thin cloud with τ=0.072 (bottom left panel), and thick cloud with τ=2.7 (bottom right panel). All spectra are from the Volume 9 South Pole data set and were recorded in 1999 before collector modification. All panels of Figure S5 show (i) the ratio of uncorrected spectra to the clear sky model; (ii) $f_G(\theta,\lambda,\tau)$; and (iii) the ratio of corrected spectra to clear sky model. The two bottom panels additionally include (iv) the ratio of corrected spectra to the cloud model. At the longest wavelengths, the uncorrected clear sky spectra deviate from the model by up to 20%. Deviations for wavelengths in the UV are typically smaller than 10%. The corrected spectra agree to within about 5% with the model. The monochromator's Wood anomaly, which is apparent in the top right panel at 505 nm, is removed by the correction. This anomaly is only visible in uncorrected spectra during clear-sky and thin-cloud conditions. The fact that the correction of this anomaly diminishes by the correct amount as cloud optical depth increases is an indication that the dependence of $R(\theta,\lambda,\tau)$ on τ is correctly estimated by the algorithm.

The ratio of corrected measurement to clear-sky model is smaller for spectra measured under cloudy skies, as one would expect. The ratio of the corrected spectrum to the cloud model is close to unity for all wavelengths for both cloud cases. The agreement at 450 nm is self-evident, as this was the wavelength used for the determination of cloud optical depth. The fact that there is good agreement at other wavelengths gives further confidence in the accuracy of the algorithm. In the case of a thick cloud, the correction consists of multiplying the measured spectral irradiance by $1/f_D = 1/0.97$. The comparison of the ratios for cases (iii) and (iv) confirms that clouds attenuate less in the UV than in the visible.

S2.4. Bandwidth Normalization

The bandwidth of SUV-100 spectroradiometers varies between 1.0±0.1 nm in the UV-B and 0.8±0.1 nm in the visible. Processing of Version 2 involved the normalization of all spectra to a uniform bandwidth of 1.0 nm. A normalized spectrum $E_N(\lambda)$ is calculated by:

$$E_N(\lambda) = \frac{E_O(\lambda)\ \ E_1(\lambda)}{E_b(\lambda)} \tag{S7}$$

where $E_O(\lambda)$ is spectral irradiance of the original spectrum,
$E_1(\lambda)$ is the extraterrestrial spectrum convolved with a triangular function of 1.0 nm FWHM,
$E_b(\lambda)$ is the extraterrestrial spectrum convolved with a triangular function of b nm FWHM.

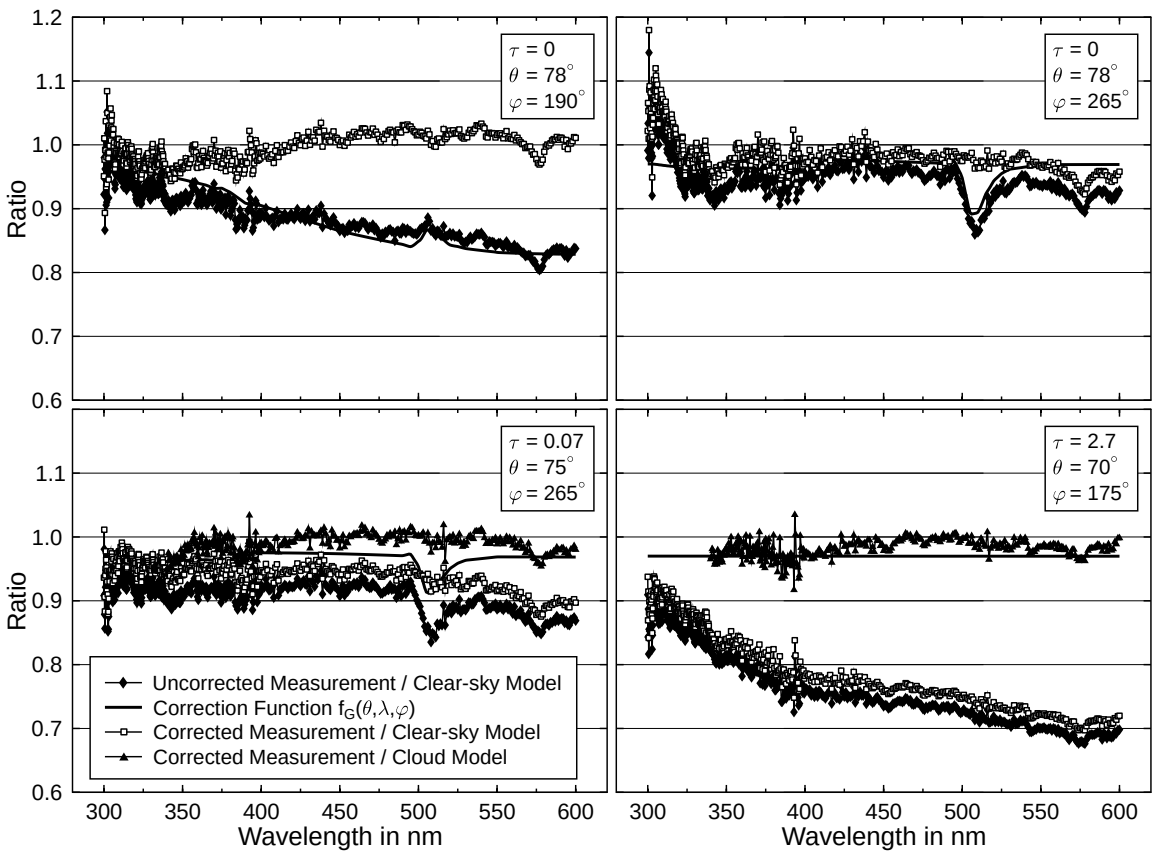

Figure S5: Comparison of measured and modeled spectra, before and after correction, for different cloud optical depths and azimuth angles. Top left: Clear sky, φ = 190°. Top right: Clear sky, φ = 265°. Bottom left: Thin cloud (τ=0.072), φ = 265°. Bottom right: Thick cloud (τ=2.7), φ = 175°.

The convolution bandwidth *b* is incremented in steps of 0.05 nm and $E_N(\lambda)$ is calculated in separate wavelength sections where the bandwidth of the original spectrum is to within ±0.025 nm of *b*. An increment of 0.05 nm is sufficiently small to avoid obvious steps at the border of neighboring sections. Results further indicate that the simplification of using triangular functions for the construction of $E_b(\lambda)$ rather than the actual SUV-100 band shape [*Bernhard et al.*, 2003a] is adequate. The algorithm only removes bandwidth effects related to the Fraunhofer structure in measured spectra. It does not remove bandwidth effects related to the slope of the spectrum in the ozone cut-off region [*Bernhard and Seckmeyer*, 1999] or the structure from the Huggins band of the ozone absorption cross section. Fortunately, the bandwidth of the SUV-100 spectroradiometers is already close to 1.0 nm in these spectral regions, and a correction is not required.

S2.5. Wavelength Resampling

After wavelength correction, spectra are given on an uneven wavelength grid, which may change from one spectrum to the next. Below 340 nm, where measured spectra were generally oversampled, the resampling was accomplished via cubic spline interpolation. Above 340 nm, resampling was done by overlaying the Fraunhofer fine structure. This is possible as the atmospheric transmission varies smoothly between 340 and 600 nm. The method is also able to fill-in the Fraunhofer structure in Volume 2 spectra from February and March 1991, which were sampled in 5.0 nm increments in the visible. The resampled spectral irradiance, $E_E(\lambda_E)$, at "even" wavelength λ_E is calculated from the normalized spectrum $E_N(\lambda)$ by:

$$E_E(\lambda_E) = \frac{E_N(\lambda)\ \ E_1(\lambda_E)}{E_1(\lambda)} \tag{S8}$$

For this calculation $E_N(\lambda)$ is taken at wavelength λ of the normalized spectrum that is closest to λ_E.

S3. Uncertainty budget

Uncertainties are calculated in accordance with the *International Standards Organization* (ISO) [1993], and *Taylor and Kuyatt* [1994], following the procedure

outlined by *Bernhard and Seckmeyer* [1999]. If not otherwise stated, standard uncertainties refer to the 1σ level. During specific periods, the uncertainty of the measurements may be higher as noted in the following. These periods are identified in Network Operation Reports [e.g. *Bernhard et a*l., 2003a], and affected spectra are also marked in Version 2 data files.

S3.1 Radiometric Calibration and Stability

Uncertainties related to the radiometric calibration are summarized in Table S1 and explained below.

The SUV-100 spectroradiometer is calibrated with 200-Watt tungsten halogen lamps of type Q6.6AT4/5CL from General Electric that have been calibrated by Optronic Laboratories Inc. (OLI) against 1000-Watt standards of spectral irradiance of type FEL. The calibration of these FEL standards is traceable to the National Institute of Standards and Technologies (NIST) source-based spectral irradiance scales from 1990. The expanded uncertainty (coverage factor k=2) of this scale is 1.8% at 250 nm, 1.1% at 350 nm, and 0.9% at 655 nm [*Yoon et al*., 2002]. Several studies have indicated that standard lamps disseminated by standards laboratories [e.g. *Walker et al*., 1987], may disagree with each other beyond their stated accuracy [*Kiedron et al*., 1999; *Gröbner et al*., 2002; *Bernhard and Seckmeyer*, 1999]. As we have no evidence that the calibrations of the FEL lamps used by OLI disagree beyond the stated accuracy from the 1990 NIST scale, we used the NIST uncertainty specification without modification. If the recently released detector-based NIST scale [*Yoon et al*., 2002] had been used for the generation of Version 2 data, spectral irradiance would be higher by approximately 1.5% at 300 nm, 1.1% at 400 nm, and 0.8 – 1% in the visible.

According to OLI calibration reports, the transfer of the calibration from the NIST FEL standard to 200-Watt lamps involves an additional uncertainty of 1.1% between 250 and 350 nm, and 0.8% between 350 and 650 nm.

Values stated in OLI calibration reports are specified in 10 nm steps. We interpolated these values to intermediate wavelengths by fitting a Planck function to the data points. This fit method leads to uncertainties of about 0.5% (see [*Bernhard et al*., 2003a]) as actual lamp spectra deviate from a Planck function. The interpolation uncertainties could have been slightly reduced by using a spline rather than a Plank function [*Bernhard and Seckmeyer*, 1999]; a Planck function multiplied with a polynomial term as fit function [*Walker et al*., 1987]; or more sophisticated functions [*Huang et al*., 1998]. Applying one of these method would have meant to re-process all calibrations from the last 12 years. We decided that the expected uncertainty reduction did not justify the extra effort.

For calibration of the SUV-100 spectroradiometer, a specially designed lamp holder equipped with a 200-Watt standard is mounted over the instrument's collector every two weeks. By measuring consecutively the signal of this lamp and a 45-Watt lamp internal to the SUV-100, the calibration of the 200-Watt standard is transferred to the internal lamp. The responsivity of the SUV-100, which is ultimately required to convert raw-signal solar spectra to calibrated solar spectra, is determined on a daily basis utilizing measurements of the internal 45-Watt lamp. By basing the responsivity on measurements of the internal lamp rather than 200-Watt standards, sensitivity drifts of the instrument between bi-weekly calibrations with 200-Watt standards are corrected.

There are three 200-Watt standards at every network location and they are used in rotation. The calibration assigned to the internal 45-Watt lamp is typically the average from several calibration events with different 200-Watt standards. This procedure reduces noise as well as uncertainties if one of the three 200-Watt standards has drifted. The calibration of the three on-site standards are verified with "traveling" standards once per year. On-site standards that appear to have drifted are either recalibrated or exchanged. The uncertainty caused by drifts of on-site standards was estimated to be 2% by reviewing Network Operations Reports. The stability of the internal 45-Watt lamp is monitored with a filtered photodiode. If measurements of this sensor indicate that the lamp has drifted by more than 2%, a new calibration is assigned to the lamp. The calibration procedure is described in detail in [*Bernhard et al*., 2003a], and associated uncertainties are detailed in the following paragraph.

A cylindrical barrel with a blackened inner wall is placed over 200-Watt standards during calibrations to screen out ambient light, and protect the lamp from wind or other environmental factors. Measurements indicate that stray light from diffuse reflections either from the barrel or lamp holder is between 0.1 and 0.3% of the measured signal. The nominal distance between the standard and the instrument's collector is 50 cm. The uncertainty of the distance is 1.0 mm, causing a 0.4% uncertainty in irradiance. Uncertainties due to other alignment errors are likely smaller than 0.2% [*Bernhard and Seckmeyer*, 1999]. The air within the barrel is not temperature stabilized. Calibrations in an environmental chamber at 30°C and –20°C did not show a significant temperature dependence. Moreover, calibrations performed during polar night at the South Pole, when ambient temperatures are as low as –70°C, are not systematically different from calibrations during January, when typical temperatures range between –20 and –30°C.

Both 200-Watt and 45-Watt lamps are operated at a current of 6.5 A. The current is monitored with high-accuracy shunts and voltmeters, which are frequently recalibrated. The uncertainty of the current measurement is 0.05%, which leads to an irradiance uncertainties of 0.5% at 300 nm and 0.25% at 600 nm. The lamp power supply is digitally controlled and the output current can only be adjusted in steps of 0.0044 A, leading to an additional uncertainty of 0.25% at 300 nm and 0.13% at 600 nm. The calibration protocol for shunts and voltmeters was less rigorous prior to 1995, leading to somewhat increased (but hard to quantify) uncertainties.

Table S1. Standard uncertainty (k=1) of radiometric calibration.

Error Source	Relative Uncertainty in %		
	310 nm	400 nm	600 nm
NIST spectral irradiance scale from 1990	0.7	0.5	0.5
Transfer from NIST FEL lamps to OLI 200-Watt lamps	0.5	0.4	0.4
Interpolation calibration certificates	0.5	0.5	0.5
Drift (or discrepancy) of 200-Watt site standards	2.0	1.5	1.5
Drift of internal 45-Watt lamp	1.2	1.0	1.0
Straylight in calibration setup	0.06	0.06	0.06
Distance 200-Watt lamp – collector SUV-100	0.4	0.4	0.4
Alignment errors	0.2	0.2	0.2
Calibration shunt and voltmeter for lamp current measurement	0.5	0.35	0.25
Resolution power supply during 200-Watt lamp scans	0.25	0.18	0.13
Resolution power supply during 45-Watt lamp scans	0.25	0.18	0.13
Drift of SUV-100 responsivity to within one day	0.3	0.3	0.3
Wavelength error during calibrations	0.31	0.16	0.04
Combined uncertainty of radiometric calibration and stability	2.7	2.1	2.1

Lamp scans are subject to a wavelength uncertainty of 0.1 nm. This uncertainty is more than double the uncertainty for solar scans, as lamp scans are not corrected with the Fraunhofer line correlation algorithm. This leads to calibration uncertainties of 0.35% at 300 nm; 0.31% at 310 nm, 0.16% at 400 nm and 0.04% at 600 nm.

S3.2. Cosine Error Correction

We use the following notation in this section: the absolute uncertainty associated with a quantity X is denoted $u(X)$; relative uncertainty is denoted $u_R(X)$ and defined as $u_R(X) = u(X)/X$.

The uncertainty $u(f_G)$ of the cosine error correction factor f_G was determined by differentiating Eq. (S3) as suggested by *Bernhard and Seckmeyer* [1999]:

$$u(f_G) = \sqrt{[R\ u(f_B)]^2 + [(f_B - f_D)\ u(R)]^2 + [(1-R)\ u(f_D)]^2} \quad \text{(S9)}$$

The values of the uncertainty terms $u(f_B)$, $u(R)$, and $u(f_D)$ are discussed in the following; the same values were applied to data from all years.

For a SZA smaller than 70º, the uncertainty $u(f_B)$ of the cosine error f_B was estimated from the variability of measurements with the cosine test apparatus performed at different years and sites (Figure S2). Beyond 70º, the uncertainty was estimated from the variation of the cosine error parameterization coefficient $a(\theta,\lambda)$ established for different years and wavelengths. Based on these estimates, $u_R(f_B)$ was set to <1.5% for SZA<30º; 1.5% for $30 \le \text{SZA} \le 60$; 2% for SZA<70º; 4% for SZA=80º; and 7% for SZA=85º.

The uncertainty $u(R)$ of the direct/global ratio $R(\lambda)$ under clear skies was estimated from the difference of $R(\lambda)$ calculated for aerosol optical depths $\tau_A = 0$ and $\tau_A = 0.02$. The choice of this range considers that model estimates of $R(\lambda)$ were based on $\tau_A = 0$, whereas measured background aerosol optical depth at the South Pole varies between 0.012±0.005 [*Shaw*, 1982] and 0.025±0.03 [*CMDL*, 2002]. (Note that CMDL optical depths were performed with a wideband pyrheliometer in the visible and have a 2 to 3 times poorer accuracy than sunphotometer-derived values, according to *CMDL* [2002].) Based on these considerations, $u_R(R)$ was calculated to be 4.1% at SZA=65º, 6.0% at SZA=75º, 8.3% at 80º, and 17.0% at SZA=85º. These values were also applied to cloudy conditions as the value of the relative uncertainty $u_R(R)$ has little impact on the overall uncertainty $u(f_G)$ when clouds reduce the direct contribution $R(\lambda)$ to near zero.

The uncertainty $u(f_D)$ of the diffuse cosine error f_D is caused by the assumptions that sky radiance is unpolarized and isotropic. These assumptions are justified in the UV- B, however in the UV-A, sky radiance can vary by up to a factor of 10 depending on direction [*Blumthaler et al*., 1996]. Systematic errors in f_D due to assumption of isotropy have been quantified by *Gröbner et al*. [1996], *Landelius and Josefsson* [2000], and *Kuchinke and Nunez* [2003], and found to be as high as 10% in extreme cases. The results of these two studies are based on the cosine error of the spectroradiometer fore-optics used by the three groups, and cannot be applied to this paper without modifications. We adopted the procedure by *Landelius and Josefsson* [2000] by calculating the radiance distribution $L(\theta,\lambda)$ at the South Pole under various conditions with the radiative transfer model, and calculated the non-isotropic diffuse cosine error $f_D^*(\lambda)$:

$$f_D^*(\lambda) = \int_{(2\pi)} L(\theta,\lambda)\, f_B(\theta,\lambda)\cos(\theta)d\Omega \Big/ \int_{(2\pi)} L(\theta,\lambda)\cos(\theta)d\Omega \quad \text{(S10)}$$

Table S2. Standard Uncertainty (k=1) Caused by Cosine Error as a Function of SZA, Wavelength λ and Cloud Optical Depth τ.

				$\tau = 0$			$\tau = 0.2$			$\tau = 1.0$			$\tau = ?$
SZA [deg]	λ [nm]	f_B	f_D	R	f_G	$u_R(f_G)$	R	f_G	$u_R(f_G)$	R	f_G	$u_R(f_G)$	$u_R(f_G)$
							Volume 7						
70	310	0.97	0.981	0.18	0.978	0.7%	0.11	0.979	0.6%	0.01	0.981	0.7%	1.0%
70	400	0.97	0.981	0.55	0.973	1.1%	0.33	0.976	0.8%	0.04	0.980	0.7%	1.4%
70	600	0.97	0.981	0.89	0.967	1.8%	0.54	0.973	1.1%	0.06	0.980	0.7%	2.1%
80	310	0.95	0.981	0.03	0.980	0.7%	0.01	0.981	0.7%	0.00	0.981	0.7%	0.9%
80	400	0.95	0.981	0.34	0.971	1.4%	0.12	0.977	0.8%	0.00	0.981	0.7%	1.7%
80	600	0.95	0.981	0.83	0.956	3.3%	0.33	0.971	1.4%	0.00	0.981	0.7%	3.5%
85	310	0.94	0.981	0.00	0.981	0.7%	0.00	0.981	0.7%	0.00	0.981	0.7%	0.9%
85	400	0.94	0.981	0.12	0.976	1.1%	0.01	0.980	0.7%	0.00	0.981	0.7%	1.3%
85	600	0.94	0.981	0.72	0.953	5.0%	0.11	0.977	1.0%	0.00	0.981	0.7%	5.1%
							Volume 10						
70	310	0.90	0.954	0.18	0.944	0.7%	0.11	0.948	0.7%	0.01	0.953	0.7%	1.0%
70	400	0.90	0.954	0.55	0.923	1.2%	0.33	0.936	0.9%	0.04	0.952	0.7%	1.9%
70	600	0.90	0.954	0.89	0.904	1.8%	0.54	0.923	1.2%	0.06	0.951	0.7%	2.8%
80	310	0.77	0.954	0.03	0.949	0.7%	0.01	0.952	0.7%	0.00	0.954	0.7%	1.0%
80	400	0.77	0.954	0.34	0.892	1.5%	0.12	0.932	0.9%	0.00	0.954	0.7%	2.7%
80	600	0.77	0.954	0.83	0.802	3.6%	0.33	0.893	1.5%	0.00	0.953	0.7%	6.2%
85	310	0.65	0.954	0.00	0.954	0.7%	0.00	0.954	0.7%	0.00	0.954	0.7%	0.9%
85	400	0.65	0.954	0.12	0.917	1.3%	0.01	0.950	0.8%	0.00	0.954	0.7%	2.0%
85	600	0.65	0.954	0.72	0.738	6.7%	0.11	0.920	1.3%	0.00	0.954	0.7%	9.6%
							Volume 12						
70	310	0.85	0.941	0.18	0.924	0.7%	0.11	0.931	0.7%	0.01	0.940	0.6%	1.2%
70	400	0.85	0.941	0.55	0.892	1.3%	0.33	0.912	1.0%	0.04	0.938	0.7%	2.4%
70	600	0.85	0.941	0.89	0.862	1.8%	0.54	0.893	1.3%	0.06	0.935	0.7%	3.8%
80	310	0.69	0.941	0.03	0.933	0.7%	0.01	0.938	0.7%	0.00	0.941	0.7%	1.0%
80	400	0.69	0.941	0.34	0.855	1.7%	0.12	0.910	1.0%	0.00	0.940	0.7%	3.5%
80	600	0.69	0.941	0.83	0.730	4.0%	0.33	0.856	1.8%	0.00	0.940	0.7%	8.4%
85	310	0.51	0.941	0.00	0.940	0.7%	0.00	0.941	0.7%	0.00	0.941	0.7%	0.9%
85	400	0.51	0.941	0.12	0.888	1.7%	0.01	0.934	0.9%	0.00	0.941	0.7%	2.7%
85	600	0.51	0.941	0.72	0.629	9.4%	0.11	0.891	1.7%	0.00	0.941	0.7%	14.0%

We estimated the uncertainty $u(f_D)$ as

$$u(f_D) = \sqrt{[u(f_D^*(\lambda))]^2 + [\frac{1}{2\sqrt{3}}(f_D - f_D^*)]^2 + [u_P(f_D)]^2}\ , \tag{S11}$$

where $u(f_D^*(\lambda))$ is the uncertainty of $f_D^*(\lambda)$ associated with the uncertainty of f_B in Eq. (S10). The term $f_D - f_D^* / 2\sqrt{3}$ is based on the assumption that the true value of the diffuse cosine error lies between f_D and f_D^*. $u_P(f_D)$ is the uncertainty due to a possible dependence of the angular response on polarization and the fact that sky radiance is polarized. We estimated $u_P(f_D)$ to be 0.5% based on an investigation by *Kiedron and Michalsky* [2003], indicating that maximum systematic errors caused by polarization effects are smaller than 1% for SZAs larger than 50° and instruments that use PTFE diffusers similar to the one of the SUV-100.

As described in Section S2.3.3., cloud optical depth is estimated from the attenuation of global irradiance at 450 nm. During periods with variable or "broken" clouds, this once-per-spectrum observation leads to large uncertainties of the cosine correction due to its dependence on $R(\lambda)$. This is particularly the case when periods with clouds in front of the Sun alternate with periods when the Sun is unobstructed. In this case, the uncertainty $u(f_G)$ of the cosine correction is expressed by:

$$u(f_G) = \sqrt{[u(f_G^{CS})]^2 + [u(f_D)]^2 + [\frac{1}{2\sqrt{3}}(f_G^{CS} - f_D)]^2} \tag{S12}$$

where f_G^{CS} is the cosine correction factor for clear sky (Eq. (S9)), and $f_G^{CS} - f_D$ describes is the difference of the clear sky and overcast sky correction factors.

The uncertainty of the cosine correction has been calculated for various conditions. In Table S2, $u(f_G)$ is compiled for SZA=70°, 80°, and 85°; λ=310, 400, and 600; cloud optical depth τ=0, 0.2, 1.0, and unknown ("τ=?") sky condition; and cosine errors f_B of Volumes 7 (smallest cosine error of all volumes), 10, and 12 (largest cosine error). The following conclusions can be drawn from the data in Table S2:

- The relative uncertainty $u_R(f_G)$ varies between 0.6 and 14.0%, depending on SZA, λ, τ and volume.
- Uncertainties increase with increasing wavelength and increasing SZA due to increased contribution from the direct solar beam: $u_R(f_G)$ varies between 0.6% and 1.0% at 310 nm; between 0.7% and 2.7% at 400 nm; and between 0.7% and 14.0% at 600 nm.
- $u_R(f_G)$ decreases with increasing cloud optical depth. For τ=1.0, less than 6% of global irradiance stems from the direct beam, and the uncertainty is almost entirely determined by $u(f_D)$. At SZA=85°, the change from τ=0 to τ=0.2 reduces the direct contribution $R(\lambda)$ from 0.72 to 0.11, leading to a reduction of $u_R(f_G)$ from 9.4% to 1.7% (see Volume 12). The effect of optically thin clouds on the spatial redistribution of radiation is therefore the most important source of error in Version 2 data.
- $u_R(f_G)$ is smallest for Volume 7 data and largest for Volume 12 data as these volumes have the smallest and largest cosine error f_B, respectively. However, data of Volumes 10-12 have a smaller azimuthal dependence (Section S3.3.), which partly compensates for the increased uncertainty $u(f_G)$.
- Total ozone column has only a minor influence on f_G and the associated uncertainty $u(f_G)$.

Eruptions of Mount Pinatubo and Cerro Hudson in June and August 1991 [*Hofmann et al*., 1992; *Self et al*., 1996] lead to elevated aerosol optical depths at the South Pole between September 1991 and end of 1994 [*Dutton and Christy*, 1992; *CMDL*, 2002]. As the cosine correction algorithm assumes an aerosol free atmosphere, reduced radiation levels during the affected period are interpreted as attenuation by clouds. To quantify the uncertainty caused by the misrepresentation of aerosol attenuation by cloud attenuation, we corrected several spectra measured during the austral spring of 1991 during cloud-free periods with the standard algorithm outlined in Section S2.3.3. and a modified algorithm, which attributed attenuation to aerosols rather than clouds, and compared the results. The two results of the two algorithms differed by less than 0.5%, indicating that the standard method is also reasonably accurate for periods with increased atmospheric aerosol loading at the South Pole.

As outlined in Section S2.3.2., the cosine error f_B is deduced by comparing measurement and model at 600 nm during clear sky periods. This method could not be applied to data measured between September 1991 and January 1993 due to the large uncertainty of aerosol attenuation. For this period, we applied the same coefficients $a(\theta,\lambda)$ for the parameterization of f_B in Eq. (S4) that we had used for the period February – March 1991. We believe that this approach is justified: first, there is no evidence that f_B had changed between March and September 1991, and during 1992, and second, corrected data do not show a step-change coinciding with the times of the instrument services in December 1991 and January 1993, when f_B could have changed.

S3.3. Azimuthal Error

The cosine error correction removes most of the azimuthal dependence of the cosine error but does not eliminate errors of higher order, which have a periodicity of $\sin(n\varphi)$ with n>1. Note that collector leveling errors, which are in the order of ±0.15°, are proportional to $\sin(\varphi)$, and are mostly removed by the cosine correction. Uncertainties due to residual azimuthal errors in corrected data were quantified by analyzing the amplitude of periodic diurnal variations in the ratio of measurement and model at fixed solar zenith angle during clear-sky periods. Uncertainties vary between 0.0% and 3.8% depending on wavelength and volume, and are compiled in Table S3. The uncertainty disappears under cloud conditions.

Table S3. Standard uncertainty (k=1) of azimuthal errors.

Volume	Period	Relative Uncertainty in %		
		330 nm	400 nm	600 nm
2	Feb 91 - Dec 91	1.1	1.9	2.9
3	Dec 91 - Jan 93	0.5	1.9	3.0
4	Jan 93 - Jan 94	0.5	1.4	2.5
5	Jan 94 - Jan 95	0.7	1.0	1.7
6A	Jan 95 - Jan 96	0.4	0.5	1.6
6B	Jan 96 - Jan 97	0.0	0.0	1.7
7	Jan 97 - Jan 98	0.0	0.4	0.7
8	Jan 98 - Jan 99	0.0	0.3	1.1
9	Jan 99 - Jan 00	0.3	0.5	1.5
10	Jan 00 - Jan 01	0.3	0.5	0.7
11	Jan 01 - Jan 02	0.4	0.5	0.7
12	Jan 02 - Jan 03	0.0	0.5	0.5
Average		0.3	0.8	1.5

S3.4. Spectral Resolution

The finite bandwidth of practical spectroradiometers leads to overestimation of the solar spectrum in the UV-B. This effect has been has been extensively discussed by *Bernhard and Seckmeyer* [1999], and their results are adopted here. At SZA=80°, and 250 DU, spectral irradiance is overestimated by an instrument with 1.0 nm resolution, such as the SUV-100, by 2.2% at 300, and 0.8% at 310 nm. Overestimations for biologically weighted spectra range between 0.3% (erythemal action spectrum [*McKinlay and Diffey*, 1987]) and 0.9% (DNA damaging radiation [*Setlow*, 1974]). These systematic

errors have not been corrected and contribute to the uncertainty budget. The finite resolution of the SUV-100 also leads to a "smoothing out" of the Fraunhofer lines in the solar spectrum. We did not associate an uncertainty to this effect.

S3.5. Wavelength Misalignment

All Version 2 spectra have been corrected for wavelength errors with the correlation algorithm described in Section S2.2. Residual wavelength errors of corrected spectra were determined by applying the algorithm a second time. On average, residual wavelength errors are 0.022 nm between 305 and 400 nm, 0.025 nm between 400 and 500 nm, and 0.031 nm between 500 and 590 nm. The correlation algorithm is hampered by low radiation levels at wavelengths below 305 nm. The wavelength correction for wavelengths below 305 nm is extrapolated from values above 305 nm and therefore have a larger uncertainty. We estimate the wavelength uncertainty at 300 nm to be 0.04 nm.

Results of our correlation algorithm and the one by *Slaper et al*., [1995] agree to within 0.003±0.018 nm (±1σ) (Section S2.2). *Slaper and Koskela* [1997] have determined the uncertainty of the method by *Slaper et al*. [1995] to be approximately 0.01 nm (1σ). We assumed the same uncertainty for our algorithm, and combined it in quadrature with the residual wavelength errors. The overall wavelength uncertainties are then 0.041 nm at 300 nm; 0.024 nm at 310 nm; 0.026 nm at 400 nm; and 0.033 nm at 600 nm.

We implemented Eq. (26) of [*Bernhard and Seckmeyer*, 1999] to translate wavelength uncertainties to irradiance uncertainties in the ozone cutoff region of the solar spectrum, assuming average SZA and total ozone conditions for South Pole. Resulting relative irradiance uncertainties are 3.3% at 300 nm, 0.75% at 310 nm, 0.37% for erythemal irradiance and 0.77% for DNA-damaging irradiance.

Interaction of wavelength shifts with the Fraunhofer structure of the solar spectrum leads to an additional uncertainty. This uncertainty was calculated by shifting the extraterrestrial spectrum by 0.025 nm (i.e. the approximate wavelength uncertainty of Version 2 spectra in the UV), and applying Eq. (25) of [*Bernhard and Seckmeyer*, 1999] to the ratio of shifted to unshifted spectrum. The resulting uncertainties are 0.4% between 280 and 390 nm, 1.2% between 390 and 400 nm in the vicinity of the strong Calcium Fraunhofer lines, and approximately 0.1% in the visible, where the Fraunhofer structure is less pronounced compared to the UV.

S3.6. Non-linearity

The signal of a linear radiometer should be proportional to the incident irradiance. Reasons for non-linearity include saturation of the PMT at high signal levels and artifacts introduced by range-changes of amplification electronics. According to manufacturer specifications, PMT (R269 from Hamamatsu) and amplifier electronics (VFC320 voltage-to-frequency converter from Burr-Brown) are linear to within ±0.1%. We checked several SUV-100 instruments for non-linearity by comparison with data of collocated GUV multi-filter radiometers, which provide global irradiance measurements in four approximately 10 nm wide UV bands centered at 305, 320, 340, and 380 nm [*Bernhard et al*., 2003d]. Non-linearity, if it existed in either of the instruments, would manifest itself in the ratio of measurements of the two instruments. Comparisons indicated that the upper limit of non-linearity in SUV-100 measurements is 4%. The actual uncertainty is likely smaller but this cannot be proven by this method as deviations between the two instruments can be caused by a variety of factors, in addition to non-linearity.

S3.7. Stray Light

Stray light stems from photons with wavelengths outside the wavelength range of the monochromator's slit function that are detected together with photons inside this range. The out-of-band rejection of the SUV-100's DH-10 double monochromator is $2 \cdot 10^{-9}$ at 8 band passes from the HeNe laser line at 632.8 nm with 0.1 mm slits, according to specifications of the manufacturer (Jobin-Yvon) of the DH-10. Our measurements with a HeCd laser at 325 nm indicate that out-of-band rejection is better than $1 \cdot 10^{-6}$, which was the maximum dynamic range achievable with our test setup. The true out-of-band rejection at 325 nm is likely better than $1 \cdot 10^{-6}$, but could not be proven.

Below 290 nm, where all solar radiation is filtered out by the ozone layer, the PMT current of the SUV-100 is composed of the PMT dark current, an artificially applied electronic offset, noise, and possibly a contribution from stray light. Measurements of the signal with the collector illuminated by the Sun (SZA=65°) are identical within statistical fluctuations to measurements where the collector was covered. This indicates that the stray light contribution to the dark current is negligible and no uncertainty therefore applies.

S3.8. Noise and Detection Limit

Solar spectral irradiance $E_S(\lambda)$ is calculated from PMT current during solar scans, $I_S(\lambda)$, PMT current during scans of the internal 45-Watt lamp, $I_{45}(\lambda)$, PMT dark current $I_D(\lambda)$, and spectral irradiance $E_{45}(\lambda)$ assigned to the 45-Watt Lamp by [*Bernhard et al*., 2003a]:

$$E_S(\lambda) = \frac{I_S(\lambda) - I_D(\lambda)}{I_{45}(\lambda) - I_D(\lambda)} E_{45}(\lambda) \qquad \text{(S13)}$$

The relative uncertainty $u_R(E_S(\lambda))$ of $E_S(\lambda)$ due to noise in the three PMT currents is then:

$$u_R(E_S(\lambda)) = \left\{ \frac{[u(I_S(\lambda))]^2 + [u(I_D(\lambda))]^2}{[I_S(\lambda) - I_D(\lambda)]^2} + \frac{[u(I_{45}(\lambda))]^2 + [u(I_D(\lambda))]^2}{[I_{45}(\lambda) - I_D(\lambda)]^2} \right\}^{0.5} \quad \text{(S14)}$$

where $u(I_S(\lambda))$, $u(I_{45}(\lambda))$, and $u(I_D(\lambda))$ are the uncertainties of $I_S(\lambda)$, $I_{45}(\lambda)$, and $I_D(\lambda)$, which were determined by statistical analysis of current measurements. The uncertainty of $E_{45}(\lambda)$ is not considered here as it already part of Table S1. Eq. (S14) has been evaluated at selected wavelengths and SZAs using data from several volumes. Figure S6 shows $u_R(E_S(\lambda))$ as a function of wavelengths for six SZAs. The figure is based on clear-sky data of Volume 12. Total column ozone during the selected scans was between 250 and 285 DU. For SZAs smaller than 80°, $u_R(E_S(\lambda))$ is between 1.0% and 1.8% at $\lambda = 305$; approximately 0.8% at 310 nm; and below 0.5% for $\lambda >= 320$. Measurements at 300 nm are close to the detection limit and $u_R(E_S(\lambda))$ varies between 2% and 100%, depending on SZA and total column ozone. Relative uncertainties for erythemal irradiance and DNA-damaging irradiance were calculated with Eqs. (30) and (31) of *Bernhard and Seckmeyer* [1999] and vary between 0.1% and 0.7% for SZA smaller than 80°. Figure S6 indicates that the noise-related uncertainty of erythemal irradiances remains negligible for SZAs as high as 90°. In contrast, the influence of noise on DNA-damaging irradiance increases sharply for SZAs larger than 86°.

The detection limit or "noise equivalent irradiance" (NEI) of SUV-100 spectroradiometers is limited by the resolution of the analog-to-digital converter of the amplified PMT current. NEI was calculated from the standard deviation of measured solar spectral irradiance at 285 nm. At this wavelength, all solar radiation is absorbed by the ozone layer, and measured irradiance (and its variation) is an instrumental artifact rather than solar irradiance. NEI of Version 2 South Pole data varies between 0.00025 μW/(cm² nm) and 0.00107 μW/(cm² nm), depending on volume. The average NEI is 0.00055 μW/(cm² nm); the SZA-dependence of NEI is smaller than 0.0002 μW/(cm² nm).

S3.9. Combined Uncertainty

The combined uncertainty is discussed in Section 3 of the main paper.

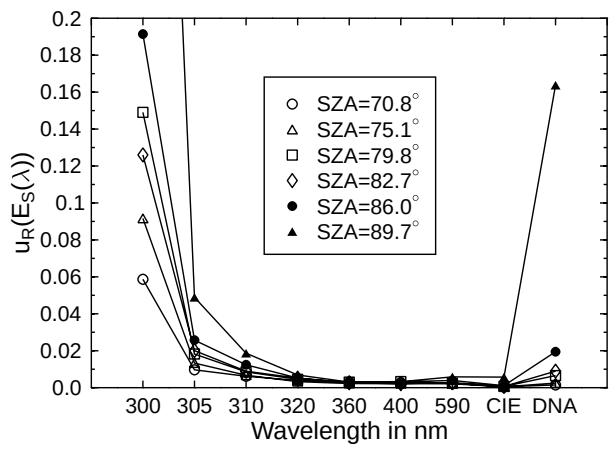

Figure S6. Relative uncertainty $u_R(E_S(\lambda))$ in solar spectral irradiance due to signal noise in calibration and solar scans. $u_R(E_S(\lambda))$ is plotted for several solar zenith angles at seven wavelengths, and for erythemal irradiance (CIE), and DNA-damaging irradiance.

S4. Comparison of Version 0 and Version 2

Figure S7 shows the ratio of Version 2 and Version 0 data as a function of time for eight different spectral integrals and dose rates $E_W(t)$, defined as:

$$E_W(t) = \int_{\lambda_L}^{\lambda_H} E(\lambda, t)\ W(\lambda)\ d\lambda$$

where $E(\lambda, t)$ is spectral irradiance at wavelength λ and time *t* and

$W(\lambda)$ is a weighting function (or action spectrum), describing the wave-length dependence of radiation on biological matter.

Spectral integrals were calculated by setting $W(\lambda) = 1$ for the wavelength ranges 298.507 – 303.03 nm, 303.03 – 307.692 nm, 307.692 – 312.5 nm, 337.5 – 342.5 nm, 290 – 315 nm (UV-B), and 400 – 600 nm. Dose rates were calculated for two weighting functions, namely the action spectrum for sunburn (erythema) [*McKinlay and Diffey*, 1987] and the action spectrum for DNA damage [*Setlow*, 1974].

Shaded bands in Figure S7 indicate data of different volumes. All time series display discontinuities at volume boundaries, as instrument maintenance performed between volumes affected the system's characteristics such as cosine error and monochromator wavelength mapping.

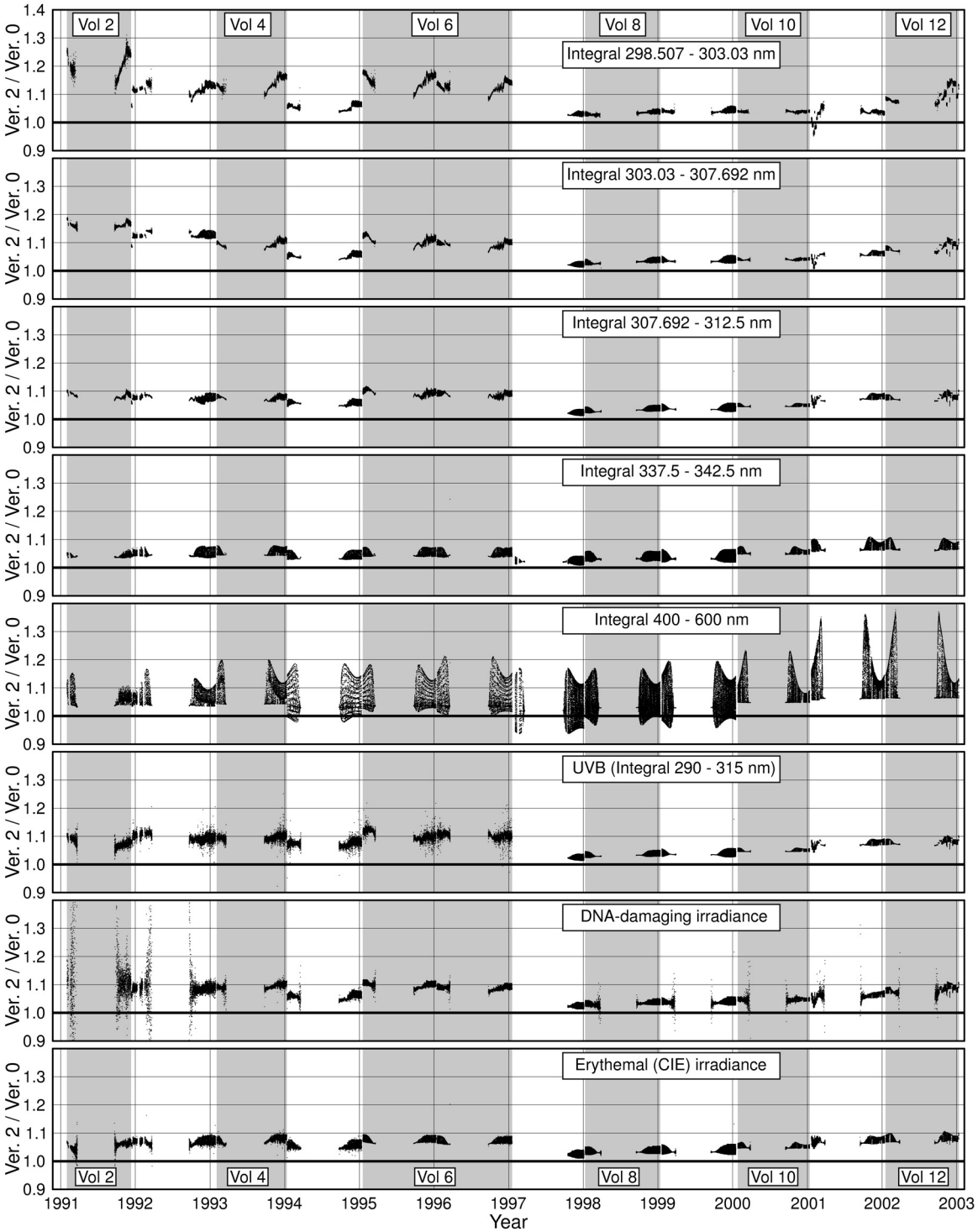

Figure S7. Ratio of Version 2 to Version 0 for the integrals 298.507 – 303.03 nm, 303.03 – 307.692 nm, 307.692 – 312.5 nm, 337.5 – 342.5 nm, 400 – 600 nm, and 290 – 315 nm; as well as DNA damaging and erythemal irradiance. Gray shading marks data that are part of even numbered Volumes as indicated on the top and bottom of the graph.

The difference between Version 0 and Version 2 is mostly caused by wavelength error and cosine error corrections. Below 310 nm, the wavelength error correction is the dominant factor due to the large increase of spectral irradiance in the ozone cut-off region of the solar spectrum. In this wavelength range, the contribution of radiation from the solar beam contributes less than 22% to global irradiance at the South Pole. The cosine error correction is therefore dominated by the diffuse correction factor $1/f_D(\lambda)$, which is smaller than 1.066 for all years, and independent of SZA.

Above 310 nm, the effect of wavelength errors is small and the difference of the two versions is almost entirely due to the cosine error correction. Differences between Version 2 and 0 peak at SZAs between 75° and 85.5°, depending on the spectral band. The decrease of the difference at large SZAs results from the diminished contribution of the direct beam to global irradiance. When the Sun is below the horizon, $f_G(\theta,\lambda)$ equals $f_D(\lambda)$ and the difference of both versions becomes small.

The change in the dominance of wavelength error and cosine error correction can be visualized by comparing the first five plots of Figure S7, which are arranged in the order of increasing wavelength.

The first plot compares Version 2 and Version 0 for the integral 298.507 – 303.03 nm. For Volumes 7-10, the difference of the two data sets is comparatively small and varies between 2% and 6%. Volume 7 was the first volume of Version 0 where the wavelength correction was based on Fraunhofer line correlation. Since results from the Version 0 and Version 2 correlation algorithms are very consistent (Section S2.1.), the application of the Version 2 wavelength correction virtually did not change the data. Most of the 2-6% difference are attributable to cosine correction. For Volumes 11 and 12, a larger number of wavelength correction functions were implemented in Version 2 than in Version 0 to better resolve drifts of the monochromator wavelength mapping observed during 2001 and 2002. This explains the larger scatter in the ratio of Version 2 / Version 0 of Volumes 11 and 12, when compared to Volumes 7-10.

For Volumes 2-6, the difference between the two versions ranges between 4% and 30% and is particularly large for Volume 2. Version 0 data of this Volume were affected by a comparatively big shift of 0.2 nm at 300 nm. Shifts in Volumes 3, 4, 5 and 6 spectra varied between 0.1 and 0.13 nm only. Volume 5 data were only shifted by 0.03 nm, and the version difference is therefore small. Errors in measured irradiance due to wavelength shifts also depend on SZA and total ozone, as both parameters influence the slope of the solar spectrum in the ozone cut-off region [*Bernhard and Seckmeyer*, 1999]. This explains why the ratio Version 2 / Version 0 of a given volume is not constant, but peaks near solstice.

The effect of the wavelength error correction is much smaller for the 303.03 – 307.692 nm integral (second plot in Figure S7) and barely noticeable for the 307.692 – 312.5 nm integral (third plot). The effect of the cosine error shows a steady increase from plot to plot and is most pronounced for the 400 – 600 nm integral. Here, differences between Version 2 and Version 0 data exceed 30%. For Volumes 2, 3, 4, 10, 11, and 12, the ratio of both versions is equal to $1/f_D(\lambda)$ during overcast periods, and rises to a larger value during clear skies, which is dependent on solar zenith and azimuth angles. The pattern of Volumes 5-9 resembles the shape of a butterfly, which can be explained by the comparatively high azimuth dependence of the instrument's angular response during this period. For some solar azimuth angles, cosine correction factors $1/f_G(\theta,\lambda)$ are smaller than $1/f_D(\lambda)$, and sometimes even smaller than unity.

The azimuth error increased significantly at the beginning of Volume 7 after the instrument had been relocated to a different building. This move has likely altered the alignment between the instrument's fore-optics and its monochromator. From Volume 10 (January 2000) onward, correction factors $1/f_G(\theta,\lambda)$ vary between $1/f_D(\lambda)$ during cloudy conditions and an upper envelope during clear-sky conditions with few values in-between during periods with optically thin clouds. The modification of the instrument's entrance optics in January 2000 reduced the heat flux to the collector, causing ice build-up underneath the diffuser on several occasions. In an attempt to increase the flux, the collector was modified again in January 2001. It is possible that the change has deteriorated the optical properties of the collector, leading to larger cosine errors and a larger difference between Version 0 and 2 for Volumes 11 and 12.

For UV-B radiation (6th plot of Figure S7), the difference between Version 2 and Version 0 is similar to that of the 307.692 – 312.5 nm integral. The UV-B ratio shows some noise for Volumes 2-6. Every SUV-100 spectrum is a composite spectrum of three raw-spectra that are measured consecutively in different, but overlapping, wavelength intervals [*Bernhard et al.*, 2003a]. For Volumes 2-6, Version 0 and Version 2 composite spectra were stitched together in a different way, and the increased noise is an artifact of the different sampling schemes.

For DNA-damaging irradiance (7th plot of Figure S7), the difference of both versions varies between 1-12%, depending on volume. Volumes 2 and 3 display larger scatter, which is rooted in the Version 0 data set. The cause is unknown. The other volumes show little intra-volume variation. The cosine error correction is dominated by the diffuse correction $1/f_D(\lambda)$ for all volumes, and contributes about 3-8% to the overall difference. The contribution of the wavelength error correction is less than 2% for Volumes 5, 7-12 and about 5% for Volumes 2, 3, 4, and 6.

For erythemal irradiance (last plot of Figure S7), the difference of both versions is less than 10%. The effect of the cosine error is slightly larger as in the case of DNA-damaging irradiance as erythemal irradiance is weighted more toward longer wavelengths. The contribution of the wavelength correction is less than 1% for Volumes 5, 7-12 and 2-3% for other volumes. Wavelength corrections for

Volumes 2 and 3 are similar, despite the difference for the 298.507 – 303.03 nm integral presented earlier, as wavelength errors of the two volumes have a different wavelength dependence between 300 and 340 nm.

S5. Comparison of Version 2 data with Model Calculations

The three extraterrestrial solar spectra $E_*(\lambda)$, $E_{\text{Gueymard}}(\lambda)$, and $E_{\text{Gueymard+Harrison}}(\lambda)$ that are discussed in the main paper are provided in ASCII format in separate files.

S6. UV Climatology at the South Pole

S6.1. Effect of Clouds on UV

Figure S8 shows the transmittance for the 400-600 nm integral as described in the main part of the paper.

S7. Discussion and Conclusions

Uncertainties in the cosine error f_B due to aerosols

At large SZAs, small changes in aerosol optical depth τ_A have a large impact on the direct-to-global ratio $R(\lambda)$, which is a crucial parameter for estimating f_B. For example, increasing τ_A from 0 to 0.02 in the model leads to a 8.3% reduction of $R(\lambda)$ at 600 nm and SZA=80º. All model calculations were performed with $\tau_A = 0$ whereas measured background aerosol optical depth at the South Pole vary between 0.012±0.005 [*Shaw*, 1982] and 0.025±0.030 [*CMDL*, 2002]. It is therefore likely that $R(\lambda)$ values determined with the model are biased high.

The SUV-100 collector is occasionally shaded by an air sampling mast, which is mounted a few meters away from the instrument. It is possible to calculate $R(\lambda)$ from a shaded spectra (i.e. the diffuse component of global irradiance) and neighboring unblocked spectra. Such calculations for spectra measured during clear skies in October 1995 at SZA=80º±1º determined R(600nm) to 0.78±0.01. Associate modeled values are 0.835±0.01, indicating that the model overestimates R(600nm) by 5-7%. Measurement and model can be brought to agreement if τ_A is set to 0.014±0.002 in the model. This value is in agreement with the measurement by *Shaw* [1982]. The tentative overestimation of $R(\lambda)$ leads to an under-estimation of f_B by 1-2%, at SZA=80º, which is within the stated uncertainty of f_B.

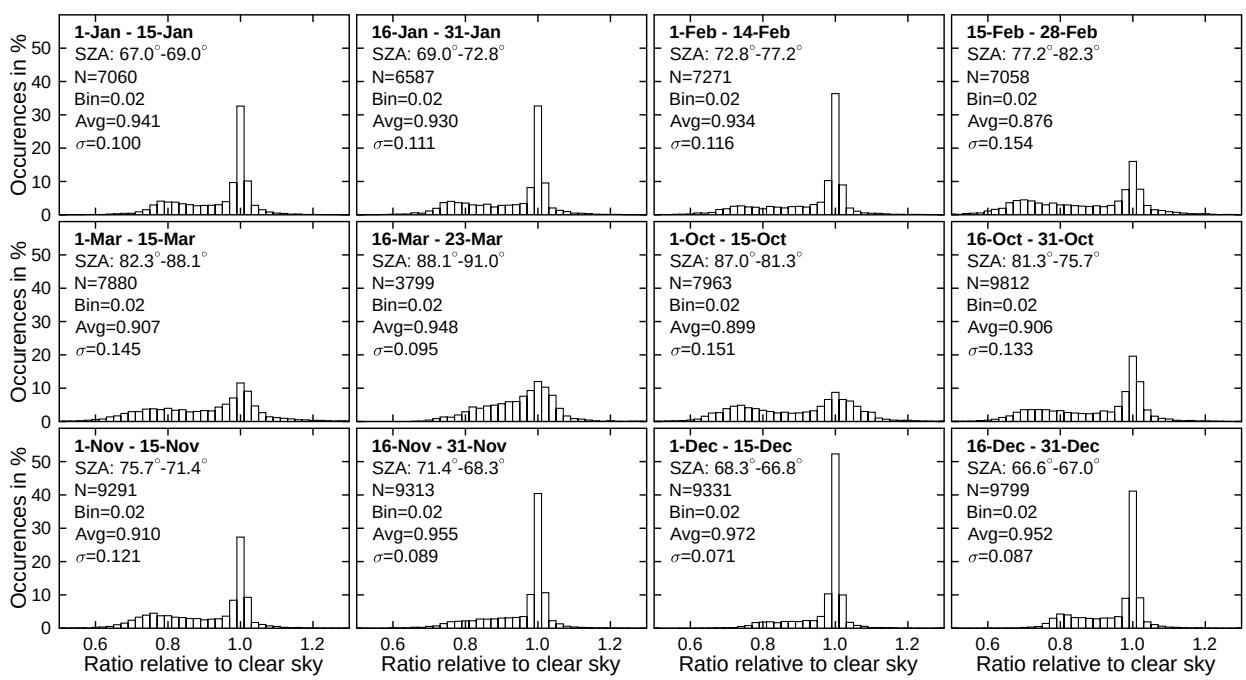

Figure S8. Frequency distributions of the ratio of spectral irradiance integrated over 400 – 600 nm to the associated clear sky irradiance. Each of the twelve plots refers to a different two-week period as indicated in the top left corner of each plot. SZA-range, number of data points N, width of the histogram columns (Bin), average (Avg), and standard deviation (σ) of the distributions are also indicated. Only data from 1994-2003 have been used.

High volcanic aerosol loading between September 1991 and March 1993 prevented estimating the cosine error from solar data of this period. The cosine error established from data of February and March 1991 was therefore applied until January 1993 (end of Volume 3). Reduction of solar irradiance by aerosols is interpreted as cloud attenuation by the cosine correction algorithm and systematic errors by the misrepresentation of aerosols by clouds were calculated to be less than 0.5% (Section S3.2). Monthly average optical depths at 450 nm determined by the correction algorithm during cloudless sky periods are 0.21±0.02 for November 1991 – January 1992, 0.09±0.01 for February and March 1992, and 0.01±0.01 for October 1992 – January 1993. Aerosol optical depth anomalies measured in the visible (530-690 nm) for the same periods by CMDL are 0.24±0.03, 0.13±0.00, and 0.12±0.03 (Figure 3.15 in [CMDL, 2002]). There is a good agreement of the two data sets between November 1991 and March 1992. However, CMDL AODs for October 1992 – January 1993 are larger than 0.1 whereas optical depth estimates from SUV-100 data are only slightly above background levels. The reason for this discrepancy is unknown. It is possible, however, that replacement of the instrument's shutter on 10/1/92 [*Booth et al*., 1993] has changed the instrument's angular response. In this case the application of the cosine correction coefficients established from the period February and March 1991 would not have been appropriate and could have lead to erroneous calculations of optical depth for the October 1992 – January 1993 period.

S8. Version 2 data products

The following data products are part of the Version 2 data set, which includes 119068 spectra. All data are provided as comma-separated text files and can be obtained at www.biospherical.com/nsf.

- High resolution spectra: data files include wavelength; time; SZA; azimuth angle; measured, corrected spectral irradiance; cosine correction; associated clear sky model spectrum; and a model spectrum where the retrieved cloud optical depth was an additional input parameter.
- Plots in PDF format comparing cosine corrected and uncorrected measured spectra with modeled spectra.
- Spectral irradiance at selected wavelengths, biologically weighted dose rates and spectral integrals over a variety of wavelength ranges (e.g. UV-B, UV-A). These data products were already part of Volume 0 (denoted database 2 and 3), but Version 2 data includes a larger number of dose rates and integrals.
- Total column ozone at times coinciding with TOMS and Dobson observations.
- Cloud optical depth at 450 nm. For the calculations, a homogeneous ice cloud layer (cirrostratus) between 5 and 6 km above sea level (2165 m – 3165 m above ground) was assumed. The effective radius was set to 20 µm. These settings are in approximate agreement with measurements performed by *Mahesh et al*. [2001] at SPO.
- Quality control flags specifying sky condition, shortest useable wavelength and associated spectral irradiance, magnitude of spikes (i.e. erratic changes of irradiance between neighboring wavelengths), residual wavelength shifts, and manual flags. Flagging is similar to that in the European UV Database, available at www.muk.uni-hannover.de/~martin/.
- Listing of model input parameters and correction parameters for every spectrum.

References

Bais, A.F., S. Kazadzis, D. Balis, C.S. Zerefos, and M. Blumthaler, Correcting global solar ultraviolet spectra recorded by a Brewer spectroradiometer for its angular response error, *Appl. Opt., 37*(27), 6339-6344, 1998.

Bais, A. F., B.G. Gardiner, H. Slaper, M. Blumthaler, G. Bernhard, R. McKenzie, A.R. Webb, G. Seckmeyer, B. Kjeldstad, T. Koskela, P. Kirsch, J. Gröbner, J.B. Kerr, S. Kazadzis, K. Leszczynski, D. Wardle, C. Brogniez, W. Josefsson, D. Gillotay, H. Reinen, P. Weihs, T. Svenoe, P. Eriksen, F. Kuik, and A. Redondas, The SUSPEN intercomparison of ultraviolet spectroradiometers, *J. Geophys. Res., 106*(D12), 12,509-12,526, 2001.

Bernhard G. and G. Seckmeyer, New entrance optics for solar spectral UV measurements, *Photochem. Photobiol., 65*(6), 923-930, 1997.

Bernhard G. and G. Seckmeyer, Uncertainty of measurements of spectral solar UV irradiance, *J. Geophys. Res., 104*(D12), 14,321-14,345, 1999.

Bernhard G., C.R. Booth, J.C. Ehramjian, V.V. Quang, and S.A. Lynch, *NSF Polar Programs UV Spectroradiometer Network 2000-2001 Operations Report*, Biospherical Instruments, San Diego, CA, 2003a, available at www.biospherical.com/NSF.

Bernhard, G., C.R. Booth, and R.D. McPeters, Calculation of total column ozone from global UV spectra at high latitudes, *J. Geophys. Res., 108*(D17), 4532, doi:10.1029/ 2003JD003450, 2003b.

Bernhard, G., C.R. Booth, J.C. Ehramjian, The quality of data from the National Science Foundation's UV Monitoring Network for Polar Regions, in: *Ultraviolet Ground- and Space-based Measurements, Models, and Effects II*, edited by W. Gao, J.R. Herman, G. Shi, K. Shibasaki, and J.R. Slusser, *SPIE Int. Soc. Opt. Eng., 4896*, 79-93, 2003c. (Also available at www.biospherical.com/nsf/presentations.asp)

Bernhard, G., C.R. Booth, J.C. Ehramjian, Real-time UV and column ozone from multi-channel UV radiometers deployed in the National Science Foundation's UV monitoring network, in: *Ultraviolet Ground- and Space-based Measurements, Models, and Effects III*, edited by J.R. Slusser, J.R. Herman, and W. Gao, *SPIE Int. Soc. Opt. Eng., 5156*, 167-178, 2003d. (Also available at www.biospherical.com/nsf)

Blumthaler, M., J. Gröbner, M. Huber, and W. Ambach, Measuring spectral and spatial variations of UVA and UVB sky radiance, *Geophys. Res. Lett, 23*(5), 547-550, 1996.

Bojkov, R.D., V.E. Fioletov, and S.B. Díaz, The relationship between solar UV irradiance and total ozone from observations over southern Argentina, *Geophys. Res. Lett., 22*(10), 1249-1252, 1995.

Booth, C.R., T.B. Lucas, T. Mestechkina, J.R. Tusson IV, D.A. Neuschuler, and J.H. Morrow, *NSF Polar Programs UV Spectroradiometer Network 1991-1993 Operations Report*, Biospherical Instruments, San Diego, CA, 1993.

Booth, C.R., T.B. Lucas, J.H. Morrow, C.S. Weiler, and P.A. Penhale, The United States National Science Foundation's polar network for Monitoring Ultraviolet Radiation, *Antarc. Res. Ser.*, edited by C.S. Weiler and P.A. Penhale, *62*, 17-37, 1994.

Booth, C.R. and S. Madronich, Radiation amplification factors: improved formulation accounts for large increases in ultraviolet radiation associated with Antarctic ozone depletion, *Antarc. Res. Ser.*, edited by C.S. Weiler and P.A. Penhale, *62*, 39-42, 1994.

Boucher, N.P., and B.B. Prézelin, Spectral modeling of UV inhibition of in situ Antarctic primary production using a field-derived biological weighting function, *Photochem. Photobiol., 64*(3), 407-418, 1996.

Chubarova, N.Y., N.A. Krotkov, I.V. Geogdzhaev, T.V. Kondranin, and V.U. Khattatov, Spectral Irradiance: the effects of ozone cloudiness and surface albedo, in: *IRS '96: Current Problems in Atmospheric Radiation*, edited by W.L. Smith and K. Stamnes, pp. 881-885, A. Deepak Publishing, Hampton, Va, 1997.

CMDL, *Climate Monitoring and Diagnostics Laboratory Summary Report No.26 2000-2001*, edited by D.B. King, R.C. Schnell, R.M. Rosson, and C. Sweet, U.S. Department of Commerce, Boulder, CO, 2002.

Cullen, J.C., P.J. Neale, and M.P. Lesser, Biological weighting function for the inhibition of phytoplankton photosynthesis by ultraviolet radiation, *Science, 258*, 646-650, 1992.

Dahlback, A., Measurements of biologically effective UV doses, total ozone abundances, and cloud effects with multichannel, moderate bandwidth filter instruments, *Applied Optics, 35*(33), 6514-6521, 1996.

Day, T., A., C. W. Grobe, and C. T. Ruhland, Impacts of climate change on Antarctic vascular plants: warming and ultraviolet-B radiation. *Antarc. J. of the U.S., Rev. 1996, 31*(2), 226-227, 1998.

Díaz, S.B., C.R. Booth, T.B. Lucas, and I. Smolskaia, Effects of ozone depletion on irradiances and biological doses over Ushuaia. *Arch. Hydrobiol. Beih: Ergebn. Limnol., 43*, 115-122, 1994.

Díaz, S.B., J.E. Frederick, T. Lucas, C.R. Booth, and I. Smolskaia, Solar ultraviolet irradiance at Tierra del Fuego: Comparison of measurements and calculations over a full annual cycle, *Geophys. Res. Let., 23*(4), 355-358, 1996.

Díaz, S.B., J.H. Morrow, and C.R. Booth, UV physics and optics; in: *The effects of UV radiation in the marine environment*, edited by , S. de Mora, S. Demers, and M. Vernet, pp. 35-71, Cambridge environmental chemistry series 10, Cambridge University Press, New York, 2000.

Díaz, S.B, G. Deferrari, C.R. Booth, D. Martinioni, and A. Oberto, Solar irradiances over Ushuaia (54.49° S, 68.19° W) and San Diego (32.45° N, 117.11° W) geographical and seasonal variation, *J. Atmos. Sol.-Terr. Phy., 63*, 309-320, 2001.

Díaz, S., D. Nelson, Don, G. Deferrari, and C. Camilión, A model to extend spectral and multiwavelength UV irradiances time series: model development and validation, *J. Geophys. Res., 108*(D4), 10.1029/2002JD002134, 2003.

Dutton, E.G. and J.R. Christy, Solar radiative forcing at selected locations and evidence for global lower tropospheric cooling following the eruptions of El Chichon and Pinatubo, *Geophys. Res. Lett., 19*(23), 2313-2316, 1992.

Early, A., A. Thompson, C. Johnson, J. DeLuisi, P. Disterhoft, D. Wardle, E. Wu, W. Mou, Y. Sun, T. Lucas, T. Mestechkina, L. Harrison, J. Berndt, and D. Hayes, The 1995 North American Interagency Intercomparison of Ultraviolet Monitoring Spectroradiometers, *J. Res. Natl. Inst. Stand. Technol., 103*(1), 15-62, 1998.

Fioletov, V.E., J.B Kerr, D.I. Wardle, N. Krotkov, and J.R. Herman, Comparison of Brewer ultraviolet irradiance measurements with total ozone mapping spectrometer satellite retrievals, *Opt. Eng., 41*(12), 3051-3061, 2002.

Frederick, J.E., and A.D. Alberts, Prolonged enhancement in surface ultraviolet radiation during the Antarctic spring of 1990, *Geophys. Res. Lett., 18*(10), 1869-1871, 1991.

Frederick, J.E., P.F. Soulen, S.B. Díaz, I. Smolskaia, C.R. Booth, T.B. Lucas and D.A. Neuschuler, Solar ultraviolet irradiance observed from southern Argentina: September 1990 to March 1991, *J. Geophys. Res., 98*(D5), 8891-8897, 1993.

Frederick, J.E. and C. Erlick, The attenuation of sunlight by high latitude clouds: spectral dependence and its physical mechanisms, *J. Atmos. Sci., 54*, 2813-2819, 1997.

Frederick, J.E, V.W. Manner, and C.R. Booth, Interannual variability in solar ultraviolet irradiance over decadal time scales at latitude 55° South, *Photochem. Photobiol., 74*(6), 771-779, 2001.

Frederick, J.E, and Y. Liao, Behavior of solar ultraviolet irradiance at high southern latitudes over decadal time scales, in: *Ultraviolet Ground- and Space-based Measurements, Models, and Effects III*, edited by J.R. Slusser, J.R. Herman, and W. Gao, *SPIE Int. Soc. Opt. Eng., 5156*, 37-47, 2003.

Gardiner, B.G., and T.J. Martin, On measuring and modeling ultraviolet spectral irradiance, in: *IRS '96: Current Problems in Atmospheric Radiation*, edited by W.L. Smith and K. Stamnes, pp. 917-920, A. Deepak Publishing, Hampton, Va, 1997.

Gröbner, J., M. Blumthaler, and W. Ambach, Experimental investigation of spectral global irradiance measurements errors due to a non ideal cosine response, *Geophys. Res. Lett., 23*(18), 2493-2496, 1996.

Gröbner, J., and J.B. Kerr, Ground-based determination of the spectral ultraviolet extraterrestrial solar irradiance: Providing a link between space-based and ground-based solar UV Measurements, *J. Geophys. Res., 106*, 7211-7217, 2001.

Gröbner, J., D. Rembges, A.F. Bais, M. Blumthaler, T. Cabot, W. Josefsson, T. Koskela, T.M. Thorseth, A.R. Webb, and U. Wester, Quality assurance of reference standards from nine European solar-ultraviolet monitoring laboratories, *Appl. Opt., 41*(21), 4278-4282, 2002.

Gurney, K. R., Evidence for increasing ultraviolet irradiance at Point Barrow, Alaska, *Geophys. Res. Lett., 25*(6), 903-906, 1998.

Harrison L., J. Michalsky and J. Berndt, Automated Multifilter Rotating Shadowband Radiometer: an instrument for optical depth and radiation measurements, *Appl. Opt.*, 33(22), 5118-5125, 1994.

Hofmann, D.J., S. J. Oltmans, J. M. Harris, S. Solomon, T. Deshler, and B. J. Johnson, Observation and possible causes of new ozone depletion in Antarctica in 1991, *Nature, 359*, 283-287, 1992.

Holm-Hansen, O., E.W. Helbling, and D. Lubin, Ultraviolet radiation in Antarctica: inhibition of primary production, *Photochem. Photobiol., 58*(4), 567-570, 1993.

Huang, L.K., R.P. Cebula, and E. Hilsenrath, New procedure for interpolating NIST FEL lamp irradiances, *Metrologia*, *35*, 381-386, 1998.

Huber, M., M. Blumthaler, and W. Ambach, A method for determining the wavelength shift for measurements of solar UV radiation, in: *Atmospheric Radiation, Proc. SPIE Int. Soc. Opt. Eng., 2049*, 354-357, 1993.

International Standards Organization (ISO), *Guide to the Expression of Uncertainty in Measurements*, ISO, Geneva, Switzerland, 1993.

Kalliskota, S., J. Kaurola, P. Taalas, J. Herman, E. Celarier and N. Krotkov, Comparison of daily UV doses estimated from Nimbus 7/TOMS measurements and ground-based spectro-radiometric data, *J. Geophys. Res.*, *105*(D4), 5059-5067, 2000.

Kaye, J.A. and T.L. Miller, The ATLAS series of shuttle missions, *Geophys. Res. Lett.*, *23*(17), 2285-2288, 1996.

Kiedron, P.W. J.J. Michalsky, J.L. Berndt, and L.C. Harrison, Comparison of spectral irradiance standards used to calibrate shortwave radiometers and spectroradiometers, *Appl.Opt*., *38*, 2432-2439, 1999.

Kiedron, P.W. and J.J. Michalsky, Measurement errors in diffuse irradiance with non-Lambertian radiometers, *Int. J. Remote Sensing*, *24*(2), 237-247, 2003.

Kuchinke and Nunez, An anisotropy correction method for all-sky measurements of diffuse UV-B erythemal irradiance, *J. Atmos. Ocean Tech*., *20*, 1523-1533, 2003.

Kurucz, R.L., I. Furenlid, J. Brault, and L. Testerman, Solar flux atlas from 296 to 1300 nm, National Solar Observatory Atlas No. 1, Harvard Univ. Press, Cambridge, Mass., 1984, available at ftp://ftp.noao.edu/fts/fluxatl/.

Ladizesky, M., Z. Lu, B. Oliveri, N. San Roman, S. Díaz, M.E. Holick and C. Mautalen, Solar ultraviolet B radiation and photoproduction of vitamin D3 in central and southern areas of Argentina., *J. Bone Miner. Res.*, *10*(4), 545-549, 1995.

Landelius T. and W. Josefsson, Methods for cosine correction of broadband UV-data and their effect on the relation between UV-radiation and cloudiness, *J. Geophys. Res*., *105*(D4), 4795-4802, 2000.

Lantz K., P. Disterhoft, E.A. Early, J. DeLuisi, A. Thompson, J. Berndt, L. Harrison, P. Kiedron, J. Ehramjian, G. Bernhard, L. Cabasug, J. Robertson, W. Mou, T. Taylor, J. Slusser, D. Bigelow, B. Durham, G. Janson, D. Hayes, M. Beaubien, and A. Beaubien, The 1997 North American interagency intercomparison of ultraviolet spectroradiometers including narrowband filter radiometers, *J. Res. Natl. Inst. Stand. Technol.*, *107*, 19-62, 2002.

Leontyeva E., and K. Stamnes, Estimations of cloud optical thickness form ground-based measurements of incoming solar radiation in the Arctic, *J. Climate*, *7*, 566-578, 1993.

Liley, J.B. and R.L. McKenzie, Time-dependent wavelength non-linearities in spectrometers for solar UV monitoring, in: *IRS '96: Current Problems in Atmospheric Radiation*, edited by W.L. Smith and K. Stamnes, pp. 917-920, A. Deepak Publishing, Hampton, Va, 1997.

Lubin, D., J.E. Frederick, C.R. Booth, T.B. Lucas, and D.A. Neuschuler, Measurements of enhanced springtime ultraviolet radiation at Palmer Station, Antarctica, *Geophys. Res. Lett.*, *16*(8), 783-785, 1989.

Lubin. D., B.G. Mitchell, J.E. Frederick, A.D. Alberts, C.R. Booth, T.B. Lucas, and D.A. Neuschuler, A contribution toward understanding the biospherical significance of Antarctic ozone depletion. *J. Geophys. Res.*, *97*(D8) 7817-7828, 1992.

Mahesh A., V.P. Walden, and S.G. Warren, Ground-based infrared remote sensing of cloud properties over the Antarctic plateau. Part II: cloud optical depths and particle sizes, *J. Appl. Meteorol*., *40*, 1279-1294, 2001.

Mayer B., *Messung und Modellierung der spektralen UV-Bestrahlungsstärke in Garmisch-Partenkirchen*, Wiss-.Verl. Maraun, Fraunkfurt am Main, Germany, 1997.

McKenzie, R. L., P. V. Johnston, M. Kotkamp, A. Bittar, and J. D. Hamlin, Solar ultraviolet spectroradiometry in New Zealand: Instrumentation and sample results from 1990, *Appl. Opt*., *31*, 6501-6509, 1992.

McKinlay, A.F. and B.L. Diffey (Eds.), A reference action spectrum for ultraviolet induced erythema in human skin, in: *Commission International de l'Éclairage (CIE), Research Note*, *6*(1), 17-22, 1987.

Nichol, S.E., G. Pfister, G.E. Bodeker, R.L. McKenzie, S.W. Wood, and G. Bernhard, Moderation of cloud reduction of UV in the Antarctic due to high surface albedo, *J. Appl. Meteorol.*, *42*(8), 1174-1183, 2003.

Palmer C., *Diffraction grating handbook*, Richardson Grating Laboratory, Rochester, New York, 2002, available at http://www.gratinglab.com.

Seckmeyer, G. and G. Bernhard, Cosine error correction of spectral UV irradiances, in: *Atmospheric Radiation, Proc. SPIE Int. Soc. Opt. Eng., 2049*, 140-151, 1993.

Seckmeyer, G., B. Mayer, G. Bernhard, R.L. McKenzie, P.V. Johnston, M. Kotkamp, C.R. Booth, T.B. Lucas, T. Mestechkina, C.R. Roy, H.P. Gies, and D. Tomlinson. Geographical differences in the UV measured by intercompared spectroradiometers, *Geophys. Res. Lett*, *22*(14), 1889-1892, 1995.

Self, S., Zhao,J-X, Holasek, R.E., Torres, R.C., and. King, A.J., The atmospheric impact of the 1991 Mount Pinatubo eruption, in: *Fire and Mud: Eruptions and lahars of Mount Pinatubo*, edited by Newhall, C. G. and Punongbayan, R.S.,Philippines Philippine Institute of Volcanology and Seismology, Quezon City and University of Washington Press, Seattle and London, 1996.

Setlow, R.B., The wavelength in sunlight effective in producing skin cancer: a theoretical analysis, *Proc. Natl. Acad. Sci. U.S.A.*, *71*(9), 3363-3366, 1974.

Shaw, G.E., Atmospheric turbidity in the polar regions, *J. Appl. Meteorol*., *21*, 1080-1088, 1982.

Slaper H., H.A.J.M. Reinen, M. Blumthaler, M. Huber, and F. Kuik, Comparing ground level spectrally resolved solar UV measurements using various instruments: a technique resolving effects of wavelength shift and slit width, *Geophys. Res. Lett.*, *22*(20), 2721-2724, 1995.

Slaper H., Methods for intercomparing instruments, in: *Advances in solar ultraviolet spectroradiometry*, edited by A.R. Webb, Air pollution research report 63, Off. for Off. Publ. of the Eur. Communities, Luxembourg, 1997.

Slaper H. and T. Koskela, Methodology of intercomparing spectral sky measurements, in: *The Nordic intercomparison of ultraviolet and total ozone instruments at Izaña, October 1996, final report*, edited by B. Kjeldstad, B. Johnsen, and T. Koskela, Finnish Meteorological Institute, Helsinki, 1997.

Smith, R.C., B.B. Prezelin, K.S. Baker, R.R. Bidigare, N.P. Boucher, T. Coley, D. Karentz, S. MacIntyre, H.A. Matlick, D. Menzies, M. Ondrusek, Z. Wan, K.J. Waters, Ozone depletion: ultraviolet radiation and phytoplankton biology in Antarctic waters, *Science*, *256*, 952-959, 1992.

Sobolev I., Effect of column ozone on the variability of biologically effective UV radiation at high southern latitudes, *Photochem. Photobiol.*, *72*(6), 753-765, 2000.

Stamnes, K., Z. Jin, J. Slusser, C.R. Booth and T.B. Lucas, Several-fold enhancement of biologically effective ultraviolet radiation levels at McMurdo Station Antarctica during the 1990 Ozone "Hole", *Geophys. Res. Lett.*, *19*(10), 1013-1016, 1992.

Taylor B.N. and C.E. Kuyatt, Guidelines for evaluating and expressing the uncertainty of NIST measurement results, *NIST Technical Note 1297, 1994 Edition*, National Institute of Standards and Technology, Gaithersburg, MD, 1994.

vanHoosier, M. E., Solar ultraviolet spectral irradiance data with increased wavelength and irradiance accuracy, in: Ultraviolet Atmospheric and Space Remote Sensing: Methods and Instrumentation, edited by R E. Huffman and C. G. Stergis, *Proc., SPIE Int. Soc. Opt. Eng., 2831,* 57-64, 1996.

Walker, J.H., R.D. Saunders, J.K. Jackson, and D.A. McSparron, Spectral irradiance calibrations, *NBS Spec. Publ. U.S., 250-20*, 1987.

Webb, A.R., B.G. Gardiner, M. Blumthaler, P. Forster, M. Huber, and P.J. Kirsch, A laboratory investigation of two ultraviolet spectroradiometers, *Photochem. Photobiol.*, *60*(1), 84-90, 1994.

World Meteorology Organisation (WMO), *Scientific assessment of ozone depletion: 1998*, Global ozone research and monitoring project, Report No. 44, Geneva, Switzerland, 1999.

World Meteorology Organisation (WMO), *Scientific assessment of ozone depletion: 2002*, Global ozone research and monitoring project, Report No. 47, 498 pp., Geneva, Switzerland, 2003.

Yoon, H.W., C.E. Gibson, and P.Y. Barnes, Realization of the National Institute of Standards and Technology detector-based spectral irradiance scale, *Appl. Opt.*, *41*(28), 5879-5890, 2002.

Zerefos C., D. Balis, M. Tzortziou, A. Bais, K. Tourpali, C. Meleti, G. Bernhard, and J. Herman, A note on the interannual variations of UV-B erythemal doses and solar irradiance from ground-based and satellite observations, *Ann. Geophys.*, *19*, 115-120, 2001.

G. Bernhard, C.R. Booth, and J.C Ehramjian, Biospherical Instruments Inc., 5340 Riley Street, San Diego, CA 92110, USA. (bernhard@biospherical.com)